Lithium isotope and mercury evidence for enhanced continental weathering and intense volcanism during the Ordovician-Silurian transition

Xiangrong Yang[a,b,c], Detian Yan[b*], David J. Wilson[c], Philip A. E. Pogge von Strandmann[c,d], Xianyi Liu[c], Chunyao Liu[c], Mu Liu[e], Liwei Zhang[b], Bao Zhang[b], Daizhao Chen[e]

[a] School of Geosciences, Yangtze University, Wuhan, 430100, China

[b] Key Laboratory of Tectonics and Petroleum Resources of Ministry of Education, China University of Geosciences, Wuhan 430074, China

[c] LOGIC, Institute of Earth and Planetary Sciences, University College London and Birkbeck, University of London, Gower Street, London, WC1E 6BT, UK

[d] MIGHTY, Institute of Geosciences, Johannes Gutenberg University, 55122 Mainz, Germany

[e] Key Laboratory of Petroleum Resources Research, Institute of Geology and Geophysics, Chinese Academy of Sciences, Beijing 100029, China

Corresponding author (Detian Yan) at: Key Laboratory of Tectonics and Petroleum Resources of Ministry of Education, China University of Geosciences, Wuhan, 430074, China. Email: yandetia@cug.edu.cn

Abstract: The Ordovician-Silurian transition (OST) was characterised by climatic fluctuations (warming in the Katian and glaciation in the Hirnantian) and mass extinctions. However, the mechanisms driving the climatic and biological variability remain under debate. In order to reveal the relationships between volcanism, climate, and continental weathering, we measured lithium (Li) isotopes and mercury (Hg) concentrations in a carbonate-dominated marine section from South China. The reconstructed $\delta^7Li_{seawater}$ values were generally ~ 21‰ during the Ordovician-Silurian transition, with negative excursions towards ~ 16‰ in the latest Katian and the latest Hirnantian intervals. We infer that changes in continental weathering affected dissolved riverine Li fluxes and δ^7Li values, and thereby exerted a major control on the seawater

δ^7Li variations, while changes in temperature that influenced isotope fractionation during weathering and reverse weathering exerted a secondary control. In the Late Katian, intense volcanic activity (high Hg/TOC ratios and low δ^{13}C values) likely initiated the climatic warming (late Boda warming), which was sustained by enhanced clay formation ($\delta^7Li_{seawater}$ values of ~21‰). The intense volcanism also contributed to the high primary productivity and expansion of ocean anoxia, accounting for the Katian extinction. In the latest Katian and latest Hirnantian, enhanced and more congruent weathering ($\delta^7Li_{seawater}$ values of 16‰) likely contributed to the initiation of global cooling and further glaciation. Meanwhile, the weathering-induced expansion of euxinic seawater could have driven the Late Ordovician Mass Extinction (LOME) events. During the Hirnantian glacial intervals, decreased and incongruent weathering could have contributed to reduced CO_2 drawdown, ultimately allowing warming and climatic recovery. Overall, the climatic fluctuations during the OST were related to changes in continental weathering, while the multi-phase biotic extinctions could be attributed to volcanism and/or weathering-induced oceanic anoxia.

Keywords: Continental weathering; Lithium isotopes; Mass extinctions; Volcanism; Glaciation

1. Introduction

During the Ordovician-Silurian transition (OST), the Earth experienced significant changes in both climatic and biotic systems (Finnegan, et al., 2011; Melchin et al., 2013; Fan et al., 2020; Kozik et al., 2022a; Qiu et al., 2022; Harper et al., 2014, 2024). The Late Ordovician Mass Extinction (LOME) was one of the most important events during the OST, and has typically been regarded as comprising two phases in the latest Katian and the late Hirnantian (Harper et al., 2014, 2024), although recent studies suggest that the major extinctions happened in the Katian (Deng et al., 2021; Harper et al., 2024). Both climatic warming (late Boda warming event in the late Katian) and cooling (glaciation in the early-middle Hirnantian) have been proposed for the Late Ordovician, based on the occurrence of glacial deposits, and from clumped-isotope analysis of carbonate rocks and fossils (e.g. Finnegan, et al., 2011; Melchin et al., 2013). Several

mechanisms (e.g. volcanism, continental weathering, organic matter burial) have been proposed to explain these extreme climates. For example, intense volcanism may have contributed to the warming climate (Wang et al., 2023), and enhanced burial of organic carbon, enhanced silicate weathering, and reduced volcanic outgassing likely resulted in the cooling climate (Finlay et al., 2010; Lefebvre et al., 2010; Lenton et al., 2012; Pogge von Strandmann et al., 2017a; Sproson et al., 2022).

Both the volcanism and continental weathering are suggested as the most important processes that can influence the climate in the geological history (Walker et al., 1981; Berner et al., 1983; Berner, 1992; McKenzie et al., 2015; Jones et al., 2017; Pogge von Strandmann et al., 2021; Deng et al., 2022; Krause et al., 2023). Large igneous provinces can release a large amount of CO_2, driving initial climatic warming (McKenzie et al., 2015; Wang et al., 2023). However, the eruption of millions of cubic kilometers of flood basalts can lead to accelerated continental weathering, which could cause long-term global cooling (Yang et al., 2018; Gernon et al., 2021). Commonly, the chemical weathering of silicate rocks is as an important process that influences or controls the global carbon cycle by removing carbon dioxide (CO_2) from the atmosphere, converting it to bicarbonate ions, and ultimately storing it in carbonates (e.g. Berner et al., 1983; Pogge von Strandmann et al., 2020). This process also releases significant amounts of nutrient elements (such as phosphorus and iron) into the ocean, with the potential to significantly influence marine primary productivity and ocean chemistry (Walker et al., 1981; Berner, 1992; Kump et al., 1999). Generally, the chemical weathering of silicate rocks involves two processes: the dissolution of primary silicate minerals and the formation of secondary minerals (Dellinger et al., 2015; Deng et al., 2022). The former process contributes to the global carbon sink (Pogge von Strandmann et al., 2020), whereas the latter process can reduce the flux of carbonate-forming cations to the oceans and lead to an accumulation of CO_2 in the atmosphere (Krause et al., 2023).

The OST was accompanied by frequent volcanic activity (Yang et al., 2019; Hu et al., 2020) and changes in continental weathering (Yan et al., 2010; Finlay et al., 2010; Lenton et al., 2012; Pogge von Strandmann et al., 2017a; Sproson et al., 2022). The

identification of volcanism during the OST is supported by petrographic and geochemical evidence (Su et al., 2009; Hu et al., 2020, 2021; Yang et al., 2019, 2022). Meanwhile, several weathering proxies, including the chemical index of alteration (CIA), and seawater strontium isotopes ($^{87}Sr/^{86}Sr$) and osmium isotopes ($^{187}Os/^{188}Os$), reveal significant changes in continental weathering processes during the OST (Yan et al., 2010; Finlay et al., 2010; Hu et al., 2017). Vigorous tectonism, intense volcanism, and climate transitions have been proposed to have induced these changes in continental weathering (Finlay et al., 2010; Buggisch et al., 2010; Pogge von Strandmann et al., 2017a; Longman et al., 2021).

Seawater lithium (Li) isotopes are a useful proxy to track continental weathering, and have been increasingly used to examine weathering changes, and their interaction with climate, in the geological past (Hathorne and James, 2006; Misra and Froelich 2012; Lechler et al 2015; Pogge von Strandmann et al., 2013, 2017a, 2021b; Kalderon-Asael et al., 2021; Sproson et al., 2022; Cao et al., 2022; Krause et al., 2023). The Li cycle is not significantly influenced by biological processes, and Li is significantly more concentrated in silicate than carbonate rocks, so Li isotopes essentially only trace silicate weathering (Kisakurek et al., 2005). In terrestrial settings, Li isotopes are significantly fractionated during chemical weathering, with the preferential retention of light Li isotopes in the solid weathering products leading to heavy Li isotope compositions in the dissolved riverine load (Pogge von Strandmann et al., 2020). The Li isotope compositions of river waters are therefore predominantly controlled by the ratio of primary rock dissolution (driving riverine δ^7Li to low, rock-like values; more congruent weathering) to the formation of secondary minerals (driving riverine δ^7Li to high values; more incongruent weathering).

Marine carbonates have generally been regarded as an effective archive for seawater δ^7Li signatures and have been widely used to reconstruct past changes in seawater compositions over a range of timescales (Misra and Froelich 2012; Pogge von Strandmann et al., 2019a; Kalderon-Asael et al., 2021; Murphy et al., 2022; Krause et al., 2023). In this contribution, we analysed Li isotopes and elemental concentrations in the upper Ordovician and lower Silurian parts of a carbonate-dominated section from

South China, with the goal of revealing the possible driving mechanisms for climate change and mass extinctions.

2. Geological setting

The South China Block was located near the equator during the Late Ordovician (Fig. 1A), and it comprised the Cathaysia Block in the southeast and the Yangtze Block in the northwest (Fig. 1B, Chen et al., 2004). Both the Cathaysia Block and the Yangtze Block were gradually uplifted from the ocean basin to form a continent, as a result of the collision between these blocks in the early Paleozoic (Fig. 1B). The northern part of the Yangtze Block formed a deep-water depressional basin as a result of crustal compression and deformation. These processes led to the wide distribution of organic-rich shales in South China, named the Wufeng and Longmaxi formations.

For this study, samples were collected from a shallow-shelf carbonate section (Wuke), spanning the Late Ordovician (late Katian and Hirnantian stages) to the Early Silurian (Rhuddanian stage). The Wuke section is situated in western Zhaojue, Sichuan Province, South China (Fig. 1B). The Wuke section can be divided into the Baota/Linxiang Formation, Tiezufeike Formation, and Butuo Formation (Liu et al., 2022a, Fig. 2). The Tiezufeike Formation mainly comprises limestone and dolomitic limestone, with the upper Tiezufeike Formation containing abundant shelly fauna (i.e. the Hirnantian fauna). The Butuo Formation comprises laminated limestone and calcareous mudstones interbedded with argillaceous siltstone and mudstone (Fig. 2).

3. Methods

3.1 Total organic carbon, total sulfur, Al_2O_3, and $\delta^{13}C_{org}$ analyses

Powdered samples were reacted with 6 M HCl to remove carbonate minerals before total organic carbon (TOC) and total sulfur (TS) analysis. The sample residues were repeatedly washed using Milli-Q water to remove HCl and finally dried in an oven overnight (50 °C). The TOC, TS, and $\delta^{13}C_{org}$ values were analysed at the China University of Geosciences, Wuhan. Approximately 100 mg of dried residue of each

sample was analysed for TOC and TS using an Elementar Vario EL, with analytical precision better than 0.1‰ for both TOC and TS. The $\delta^{13}C_{org}$ analysis was conducted using a Finnigan MAT 253 isotope ratio mass spectrometer (IRMS), with analytical precision better than ± 0.2‰.

The major elements, including Al_2O_3, were measured by X-ray fluorescence spectrometry (XRF) at Wuhan Sample Solution Analytical Technology Co., Ltd. The standard curve was prepared using the national standard materials, including rock standard GBW07101–14, soil standard GBW07401–08, and stream sediment standard GBW07302-12. The relative standard deviation (RSD) was less than 2%, and the analytical precision was better than 5%.

3.2 Lithium isotopes and elemental analyses

The exchangeable fraction of the samples was leached using 1 M sodium acetate for 1 h at room temperature (Pogge von Strandmann et al., 2019a), and then the bulk carbonate was leached in 0.1 M HCl for 1 hour. The carbonate leachate samples containing 10-40 ng Li were purified through a two-stage cation exchange chemistry using dilute HCl as the eluant, according to Liu et al. (2022b). Lithium isotope analyses were performed in the LOGIC (London Geochemistry and Isotope Centre) laboratories at University College London using a Nu Plasma 3 MC-ICP-MS. A sample-standard bracketing approach was applied using the IRMM-016 standard, which is effectively identical to the LSVEC standard (Flesch et al., 1973), with δ^7Li of LSVEC relative to IRMM-016 = -0.003 ± 0.054 (Pogge von Strandmann et al., 2019b). Analytical methods were identical to those described in Liu et al. (2022b). During this procedure, each sample was analysed three separate times. The Li isotope values are reported in permil (‰) relative to the LSVEC standard: $\delta^7Li = [(^7Li/^6Li)_{sample}/(^7Li/^6Li)_{LSVEC} - 1] \times 1000$. Accuracy and external reproducibility were determined by analyzing modern seawater (δ^7Li = 31.1 ± 0.6 ‰, n = 16), which agrees with the long-term value of seawater in this laboratory of 31.18 ± 0.38 ‰ (n = 43).

Fractions of the carbonate leachates were retained for cation analysis using an Elan Quadrupole ICP-MS and elemental ratios were determined following the methods

described by Pogge von Strandmann et al. (2013). Briefly, samples were matrix-matched to Ca concentrations and calibrated against a set of synthetic multi-element standards. The reference material JLs-1 was analysed, and indicates that accuracy and precision were better than ± 7 % for all elemental concentrations reported here.

3.3 Mercury concentration analyses

Mercury (Hg) concentrations in bulk rocks were analysed using a Direct Mercury Analyzer (DMA80) at the China University of Geosciences, Wuhan. Results were calibrated to Chinese certified reference materials GBW07404 (590 ± 50 ppb Hg) and GBW07424 (33 ± 4 ppb Hg). Data quality was monitored via multiple analyses of the standards, yielding an analytical precision (2σ) of ± 0.5% on reported Hg values.

4. Results

4.1 Carbon isotope and stratigraphic constraints

The $\delta^{13}C_{org}$ values are variable throughout the Wuke section (Fig. 2), with moderately high values in the lower Tiezufeike Formation (~ -28‰), shifts towards lower values in the middle Tiezufeike Formation (~ -30‰), and then a rise in the upper Tiezufeike Formation to reach a peak within the uppermost Tiezufeike Formation (~ -25‰). This $\delta^{13}C_{org}$ peak coincides with the incursion of an abundant Hirnantia – Dalmanitina fauna (Liu et al., 2022a), which is mainly a cold/cool-water fauna observed in the Guanyinqiao Member in deep-water shelf settings (Yan et al., 2009; Melchin et al., 2013). The $\delta^{13}C_{org}$ values fall rapidly in the lower Butuo Formation (~ -31‰), followed by increasing values in the upper Butuo Formation (~ -29‰).

Correlation of parasequences (or cycles) in the Wuke section with another shallow-water section has been cautiously conducted by Liu et al. (2022a). In their study, the Late Ordovician to Early Silurian periods, spanning from *D. complexus* to *A. ascensus* zones, have been recognised in the Wuke section. The biostratigraphy and high-resolution $\delta^{13}C$ chemostratigraphy ($\delta^{13}C_{org}$ and $\delta^{13}C_{carb}$) for the Ordovician-Silurian successions have been reported extensively (Yan et al., 2009; Melchin et al., 2013). The

$\delta^{13}C_{org}$ profiles for the Wuke section show similar trends to profiles from South China ($\delta^{13}C_{org}$) and other global Late Ordovician to Early Silurian sections ($\delta^{13}C_{org}$ or $\delta^{13}C_{carb}$) (Fig. 2). The $\delta^{13}C_{org}$ and $\delta^{13}C_{carb}$ values remain stable and high during the late Katian, aligning with the mid-Boda cooling (Melchin et al., 2013; Myrow et al., 2019). Subsequently, the $\delta^{13}C_{org}$ and $\delta^{13}C_{carb}$ values decrease in the *P. pacificus* zone, reflecting the late Boda warming interval caused by intense volcanism (Melchin et al., 2013; Myrow et al., 2019; Wang et al., 2023). Then, the $\delta^{13}C_{org}$ values become slightly more positive in the uppermost *P. pacificus* zone, which can be observed in the upper Wufeng (Wangjiawan), Tiezufeike (Wuke), upper Hartfell (Dob's Linn) and Vauréal formations (Pointe Laframboise). It is worth noting that the placement of the Katian-Hirnantian boundary in the Anticosti Island sections (Pointe Laframboise and Ellis Bay West) is under debate, with some studies suggesting that the boundary should be placed within the upper Ellis Bay Formation (Young et al., 2010; Jones et al., 2011; Kozik et al., 2022b) and others suggesting that it should be placed at the base of the Ellis Bay Formation (Melchin et al., 2013; Jones et al., 2020). In this study, we favour the view that the upper Ellis Bay Formation contains the Hirnantian boundary based on previous studies (Young et al., 2010; Jones et al., 2011; Kozik et al., 2022b). The largest positive $\delta^{13}C$ excursion (Hirnantian isotopic carbon excursion; HICE) occurs in the *M. extraordinarius* zone (uppermost Tiezufeike Formation in Wuke) or upper *M. persculptus* zone (e.g. Guanyinqiao member in Wangjiawan, upper Hartfell Shale Formation in Dob's Linn, uppermost Ellis Bay Formation in Anticosti Island sections), accompanied by a major regression and the largest Hirnantian glacial episode (Melchin et al., 2013). However, there are differences in the peak $\delta^{13}C_{carb}$ values between Wuke and other sections (e.g. Anticosti Island sections) (Fig. 2), which has been explained by marine diagenesis (Jones et al., 2020) or local carbonate weathering (Hu et al., 2017). Finally, at the start of the Silurian, the $\delta^{13}C_{org}$ and $\delta^{13}C_{carb}$ values return to lower values that are similar or slightly lower than those from before the Hirnantian glaciation, coinciding with the glacial termination and a warming climate (Melchin et al., 2013). This event can be observed in the lower Longmaxi (Wangjiawan), lower Butuo (Wuke), Birkhill (Dob's Linn), and Becscie formations (Pointe Laframboise).

4.2 Lithium isotopes in carbonates

The carbonate Li isotope data from Wuke cover a period spanning the late Katian to Rhuddanian (Table 1; Fig. 4). During the late Katian (lower-middle *P. pacificus* zone), δ^7Li values were persistently high (~ 15‰), followed by slightly lower values in the latest Katian (upper *P. pacificus* zone) (~ 12‰). High δ^7Li values occurred during the Hirnantian glaciation (*M. extraodinarius* to *M. persculptus* zones) (~ 16‰), although interrupted by anomalously low δ^7Li values in the mid Hirnantian (~ 11‰, which might have been influenced by meteoric diagenesis, as discussed below). The δ^7Li values then decreased rapidly coincident with the decreasing δ^{13}C values at the end of the Hirnantian glaciation, and remained low during the latest Hirnantian (upper *M. persculptus* zone) and earliest Rhuddanian (~ 9‰). Following this interval, the δ^7Li values quickly returned to relatively high values for the remainder of the Rhuddanian (~ 15‰).

4.3 TOC, TS, Al_2O_3, and Hg concentrations in bulk rocks

The TOC concentrations in the Wuke section range from 0.05% to 2.30%, with a mean of 0.48% (Table 2). The TOC shows low values in the Tiezufeike Formation (ranging from 0.05% to 1.39%, with a mean of 0.24%), except for two samples in the upper Tiezufeike Formation (1.04%, 1.39%). The Butuo Formation is characterised by higher TOC values (ranging from 0.11% to 2.30%, with a mean of 0.75%) than those in the Tiezufeike Formation. The TS concentrations in the Wuke section have persistently low values, ranging from 0.01% to 0.56%, with a mean of 0.24%, except for some samples in the upper Butuo Formation (higher than 0.3%).

The Al_2O_3 concentrations in the Wuke section are low throughout (ranging from 0.1% to 15.2%, average: 2.3%). The Hg concentrations in the Wuke section range from 3 ppb to 273 ppb, with a mean of 30 ppb (Table 2). The Hg concentrations in the Tiezufeike Formation range from 3 ppb to 273 ppb, with a mean of 30 ppb. The Hg concentrations in the Butuo Formation range from 3 ppb to 113 ppb, with a mean of 32 ppb. For the normalised Hg concentration proxies (Hg/TOC, Hg/TS, Hg/Al_2O_3; Fig. 4), the

baselines are calculated as the median values (63 ppb/% for Hg/TOC, 631 ppb/% for Hg/TS, and 13 ppb/% for Hg/Al_2O_3).

5. Discussion

5.1 Influence of leaching, pH, mineralogy, and diagenesis on carbonate Li isotopes

Previous leaching experiments show that the Al/Ca ratios of the leached carbonate fraction should be lower than 0.8 mmol/mol (Table 1), because above this value the silicate-derived Li can resolvably affect the Li isotope composition of carbonate samples (Pogge von Strandmann et al., 2013). In our samples, the Al/Ca ratios are all below 0.7 mmol/mol (Fig. 3A), which suggests that the effect of leaching of silicates during sample leaching is insignificant. Recently, it was proposed that samples with Al/(Ca+Mg) ratios higher than 0.45 mmol/mol can also potentially be influenced by silicate contamination (Dellinger et al., 2020). However, there is no clear relationship between Al/Ca ratios and δ^7Li_{carb} values (r=+0.26; Fig. 3A), which indicates that there is no identifiable effect of any such minimal silicate contamination on the Li isotopes measured in this study.

Manganese can be used as an indicator for the leaching of Mn oxides or oxyhydroxides (Pogge von Strandmann et al., 2013). In the Wuke section, the Mn/Ca ratios vary across the Late Ordovician to Early Silurian, with relatively low values in the latest Hirnantian. This variability likely reflects changing redox conditions during this time period (Zou et al., 2018). For the complete record, partly driven by the low Mn/Ca data from that interval, there is a weak positive correlation between Mn/Ca ratios and δ^7Li_{carb} values (r=+0.53; Fig. 3B), which could potentially indicate some effect from Mn oxyhydroxides on the measured Li isotope values. However, the Mn oxide content is expected to be lower under more anoxic water conditions, so instead we suggest that the lower Mn/Ca ratios in the sediments from the latest Hirnantian likely reflect deposition under more anoxic water conditions (high Ce/Ce*; Liu et al., 2022a), simultaneous with an interval of more congruent weathering (low δ^7Li_{carb} values; discussed below).

Moreover, it has been suggested that there is a significant pH control on Li isotopes in carbonates, with a negative correlation between pH and δ^7Li expected (~0.34‰ decrease in δ^7Li values for a pH increase of 0.1 units; Day et al., 2021). However, the latest Hirnantian corresponds to a warming climate, and likely represents an interval with low pH values due to the increased atmospheric CO_2 levels. Such a decrease in pH would be expected to generate a positive δ^7Li excursion in the latest Hirnantian, which contrasts with the observed shift to low δ^7Li values during this period (Fig. 4).

Carbonate mineralogy and diagenesis have also been proposed to influence the Li isotope compositions of bulk carbonates (Dellinger et al., 2020; Murphy et al., 2022; Wei et al., 2023; Liu et al., 2023a; Wei and Zhang, 2024). Specifically, the δ^7Li values could be affected by the dominant primary carbonate mineralogy, with aragonite showing greater Li isotope fractionation from seawater than high-Mg calcite ($\Delta_{\text{aragonite-seawater}}$ = –12‰ to –9‰; $\Delta_{\text{high Mg calcite-seawater}}$ = –7‰ to –6‰; Pogge von Strandmann et al., 2019a; Wei et al., 2023). However, it is difficult to identify the primary mineralogy in Late Ordovician carbonates because aragonite and high-Mg calcite could easily transform to low-Mg calcite or dolomite during diagenesis. Multi-proxy geochemical evidence ($\delta^{44}Ca_{carb}$ and $\delta^{26}Mg_{carb}$) suggests that shallow shelf settings may have been dominated by aragonite during the Late Ordovician (Kimmig and Holmden, 2017; Jones et al., 2020), but these assumptions still lack petrographic evidence, while the global ocean has been interpreted as a "calcite sea" for the Late Ordovician (Sandberg and Hudson, 1983).

The carbonate rocks in the Wuke section are primarily composed of calcite (majority > 70%), with variable dolomite content (~1% to 50%) within the middle *P. pacificus* and *M. persculptus* biozones (Yang et al., 2021). In addition, all the carbonates in the Wuke section have lower Sr/(Ca+Mg) values (< 1 mmol/mol) compared to aragonites from the Great Bahama Bank and South China Sea (~ 6 mmol/mol; Dellinger et al., 2018, 2020). We also note that the primary mineralogy in the Pointe Laframboise (Anticosti) section was dominated by calcite, as supported by the similarity of δ^7Li values between bulk carbonate and calcitic brachiopods (Pogge von Strandmann et al., 2017a). Given the similarity of the δ^7Li values between the Wuke and Anticosti sections, we also

suggest that the primary mineralogy in the Wuke section was calcite, although evidently some calcite experienced dolomitization during diagenesis (Fig. 4).

Meteoric diagenesis could lead to variable δ^7Li values due to a wide range of Li isotope fractionation ($\Delta^7Li_{meteoric\ diagenetic\text{-}seawater}$ = –15‰ to –3‰, Dellinger et al., 2020; –5‰ to –9‰, Wei et al., 2023), but such values are often indistinguishable from those of primary carbonates in the South China Sea or the Great Bahama Bank (Dellinger et al., 2020; Wei et al., 2023). This resistance to resetting has been explained by either the low Li concentrations of the added diagenetic fluids under sediment-buffered conditions, or the similar δ^7Li values between freshwater and marine carbonates (Wei et al., 2023). Generally, meteoric diagenetic carbonates are expected to form under low sea-level conditions (James and Choquette, 1984) and to be characterised by low $\delta^{13}C_{carb}$ (–12‰ to 0‰) values, low δ^{18}O values, and low Li/(Ca+Mg) ratios (0 to 6 μmol/mol) (Dellinger et al., 2020; Wei et al., 2023). However, for the Wuke section, the temporal variability in $\delta^{13}C_{carb}$ values cannot be used to indicate meteoric diagenesis, because of the other controls on those values. The high $\delta^{13}C_{carb}$ values during the Hirnantian glaciation ($\delta^{13}C_{carb}$ ~ 2.5‰, $\delta^{13}C_{org}$ ~ –25‰; Fig. 4) are proposed to record enhanced burial of organic matter (Kump et al., 1999), while the low $\delta^{13}C_{carb}$ values during the latest Hirnantian ($\delta^{13}C_{carb}$ ~ -2‰, $\delta^{13}C_{org}$ ~ -31‰; Fig. 4), corresponding to the warming climate and glacial termination, likely reflect enhanced release of ^{13}C-depleted CO_2 and H_2S into the ocean and atmosphere due to an expansion of euxinia (Zou et al., 2018; Yang et al., 2024). It has also been suggested that highly variable δ^{18}O values (from –8‰ to +4‰) can occur in the transition between marine (from ~ +4‰) and meteoric (from ~ –8‰) diagenesis (Wei et al., 2023). Therefore, the overall low δ^{18}O values (from ~ –10‰ to ~ –7‰) throughout the Wuke section (Fig. 4; Liu et al., 2022a) could point to a possible influence from meteoric diagenesis. However, there is no correlation between the δ^{18}O and $\delta^{13}C_{carb}$ values (Liu et al., 2022a), indicating that the variations in $\delta^{13}C_{carb}$ and δ^7Li_{carb} values through the record are probably not controlled by meteoric diagenesis. We observe that four samples (w27, w28, w29, w30) within the Hirnantian glaciation are characterised by obviously low Li/(Ca+Mg) ratios (< 10 μmol/mol; Fig. 3C-D), and anomalously low δ^7Li_{carb} values (Fig. 4), which likely

indicates that these particular samples experienced some degree of meteoric diagenesis with greater Li isotopic fractionation compared to the primary calcite ($\Delta^7Li_{meteoric\ diagenetic\text{-}seawater}$ = –15‰ to –3‰, Dellinger et al., 2020; –5‰ to –9‰, Wei et al., 2023).

Marine diagenesis can contribute to the transformation of primary carbonate minerals to secondary low-Mg calcite or dolomite (Higgins et al., 2018; Dellinger et al., 2020). Therefore, it has been proposed that such early diagenetic processes could potentially significantly overprint primary δ^7Li_{carb} values (Dellinger et al., 2020; Murphy et al., 2022; Wei et al., 2023; Wei and Zhang, 2024), with seawater-buffered carbonates showing muted isotopic offsets from seawater ($\Delta^7Li_{seawater\ buffered\text{-}seawater}$ = ~ –2‰, Wei et al., 2023) and sediment-buffered carbonates showing large offsets from seawater ($\Delta^7Li_{sediment\ buffered\text{-}seawater}$ = ~ –15‰ to –8‰). Marine diagenetic carbonates could effectively archive ambient seawater compositions, with their high Li contents resulting in a seawater-buffered diagenetic regime (Dellinger et al., 2020; Wei et al., 2023). Seawater-buffered diagenesis with high fluid-rock ratios would be expected to leave δ^7Li values unchanged, while being accompanied by lower Li/(Ca+Mg) and Sr/(Ca+Mg) ratios (Fig. 3C; Dellinger et al., 2020; Murphy et al., 2022; Wei et al., 2023). In contrast, sediment-buffered diagenesis should lead to higher Li/(Ca+Mg) and Sr/(Ca+Mg) ratios accompanied by lower δ^7Li values (Dellinger et al., 2020; Jones et al., 2020; Wei et al., 2023). The majority of the Wuke samples have low Sr/Ca ratios (< 1 mmol/mol), which are lower than those for sediment-buffered diagenesis (> 2 mmol/mol) but similar to those for seawater-buffered diagenesis (Jones et al., 2020), consistent with a role for the latter process. However, there is no correlation between Li/(Ca+Mg) ratios and δ^7Li_{carb} values (r=+0.24; Fig. 3D), Sr/(Ca+Mg) ratios and δ^7Li_{carb} values (r=+0.11; Fig. 3E), or Mg/(Ca+Mg) ratios and δ^7Li_{carb} values (r=+0.24; Fig. 3F), which supports that the recorded Li isotope variations are predominantly not controlled by changes in marine diagenesis.

The studied Wuke section and previously studied sections from Anticosti Island (Pointe Laframboise and Ellis Bay West) show similar temporal patterns of δ^7Li_{carb} values during the OST (Figs. 4-5). However, in detail, there are some differences between the Wuke and Anticosti Island sections. For example, the Hirnantian peak

δ^7Li_{carb} values are ~ 3‰ lower in the Wuke section (~16‰) compared to the two Anticosti Island sections (~19‰) (Fig. 5). In addition, the δ^7Li_{carb} values in the latest Katian are ~3‰ higher in the Wuke section (~12‰) compared to the two Anticosti Island sections (~9‰) (Fig. 5). Since the calcitic brachiopods and bulk carbonates analysed in the Pointe Laframboise (Anticosti) section show similar δ^7Li_{carb} values, these carbonates do not appear to have experienced any significant degree of diagenesis (Pogge von Strandmann et al., 2017a). The Li isotope fractionation between dolomite and seawater is similar to calcite, although early diagenesis could alter the fractionation factor (Liu et al., 2023a). Based on the differences in the offsets from seawater among meteoric diagenesis ($\Delta^7Li_{carb\text{-}seawater}$ ~ –5 to –9‰, Wei et al., 2023), seawater-buffered diagenesis (~ –2‰, Wei et al., 2023), sediment-buffered diagenesis (~ –15 to –8‰, Dellinger et al., 2020), and primary mineralogy (~ –6‰, Wei et al., 2023), we attribute the lower peak δ^7Li_{carb} values for the Hirnantian glaciation of the Wuke section to possible meteoric diagenesis in those particular samples. In contrast, more seawater-buffered diagenesis for Late Ordovician carbonates could be supported by lower Sr/Ca ratios (Jones et al., 2020). In this case, the higher δ^7Li_{carb} values in the latest Katian of the Wuke section (Fig. 5) could possibly be caused by seawater-buffered diagenesis with muted Li isotopic fractionation (($\Delta^7Li_{carb\text{-}seawater}$ ~ –2‰, Dellinger et al., 2020; Wei et al., 2023) because the Sr/Ca ratios in Wuke section are generally low (< 1 mmol/mol), although more studies are needed to test these possibilities.

Finally, we note that it has been widely observed that some Upper Ordovician sections in South China exhibit negative $\delta^{13}C_{carb}$ shifts within the Hirnantian-age Guanyinqiao Bed (Chen et al., 2017, 2020). These negative $\delta^{13}C_{carb}$ values have been attributed to the incorporation of dissolved inorganic carbon derived from organic matter in the underlying (Katian-age Wufeng Formation) and overlying (Rhuddanain-age Longmaxi Formation) black shales from the deeper shelf (Chen et al., 2017, 2020). All those sections (dominated by shales and marls) were deposited deeper than the Wuke section (dominated by carbonates), where early diagenesis would have involved organic matter oxidation driven by microbial sulfate reduction and/or methanogenesis/anaerobic oxidation of methane (Chen et al., 2017, 2020). In such a

scenario, the downward fluid movement from the overlying Butuo Formation rocks into the uppermost Tiezufeike Formation would generate a negative $\delta^{13}C_{carb}$ excursion in the Hirnantian-age sediments. However, in the Wuke section, a clear positive $\delta^{13}C_{carb}$ excursion is observed within the upper Ordovician rocks (Fig. 4; Liu et al., 2022a), which is consistent with the global HICE, implying an insignificant diagenetic overprint on the $\delta^{13}C_{carb}$ record. Furthermore, the Wuke section sediments were deposited in a shallower setting than those discussed by Chen et al. (2017, 2020), with the underlying strata (Butuo Formation) showing low TOC content (majority < 1%) and the overlying strata showing low to medium TOC content (majority < 2%), making this section less susceptible to such an effect. Therefore, we suggest that the variations of $\delta^{7}Li_{carb}$ values in the Wuke section are also not controlled by Li remobilisation during diagenetic organic matter oxidation.

5.2 Influence of reverse weathering on seawater Li isotope values

Reverse weathering, involving the formation of marine authigenic clays, is widely accepted as one of the major sinks of Li from seawater, and it also influences seawater $\delta^{7}Li$ values because it preferentially removes ^{6}Li over ^{7}Li (Kalderon-Asael et al., 2021; Cao et al., 2022). The reverse weathering reaction requires reactive Si sources (thought to be derived predominantly from opal in the modern oceans), reactive Al sources, cations (e.g., Mg^{2+}, K^{+}, Na^{+}), and alkalinity (Michalopoulos and Aller, 1995; Isson and Planavsky, 2018). A long-term increase in $\delta^{7}Li_{seawater}$ values has been reported over the past 3 billion years, with low $\delta^{7}Li_{seawater}$ values during the Precambrian (6 – 16‰) evolving towards high $\delta^{7}Li_{seawater}$ values in the modern ocean (~ 31‰) (Kalderon-Asael et al., 2021). A relatively small Li isotope fractionation associated with the marine sediment sink (< 10‰) is required to explain the low Precambrian $\delta^{7}Li_{seawater}$ values, which likely reflects the high dissolved Si concentrations and rapid rates of authigenic clay formation in the absence of Si biomineralizers (Kalderon-Asael et al., 2021). Recently, several studies suggested that intense reverse weathering may also have occurred during the Late Permian and Early Triassic periods (Cao et al., 2022), and even during the Early Cenozoic (Dunlea et al., 2017). Therefore, it is important to

evaluate the potential influence of reverse weathering changes on the seawater δ^7Li evolution during our study interval.

The published Late Ordovician seawater δ^7Li values, which also include a δ^7Li excursion in the Hirnantian (Pogge von Strandmann et al., 2017a), fit with the reconstructed long-term seawater trend (Kalderon-Asael et al., 2021). Therefore, the uptake of dissolved silica into authigenic clays likely occurred at persistent high rates across the OST, with an associated small sink fractionation factor ($\Delta_{seawater\text{-}sed}$ < 10‰, Kalderon-Asael et al., 2021). Given that the temperature-dependence of this fractionation could only explain a maximum of ~2‰ change in $\delta^7Li_{seawater}$ values based on our modelling (see Section 5.4 for details), it seems that changes in reverse weathering could not have been the main driver of the variability in $\delta^7Li_{seawater}$ values during the OST.

5.3 Global changes in continental chemical weathering during the Ordovician-Silurian Transition

Bulk carbonates from the open ocean are regarded as a reliable archive of seawater δ^7Li values, which can reflect changes in global chemical weathering fluxes or regimes (Pogge von Strandmann et al., 2013, 2019a; Dellinger et al., 2020; Murphy et al., 2022; Wei et al., 2023; Wei and Zhang, 2024). Therefore, Li isotopes in marine carbonates have been used to reconstruct palaeo-weathering conditions on the continents (e.g. Hathorne and James, 2006; Misra and Froelich 2012, Lechler et al 2015, Pogge von Strandmann et al., 2013, 2017a; Kalderon-Asael et al 2021; Sproson et all., 2022). Specifically, the Li isotope compositions of river waters, which represent the most important Li flux to the ocean (Misra and Froelich, 2012), are controlled by the ratio of weathering rate to denudation rate (W/D) (Dellinger et al., 2015). Primary rock dissolution in low W/D regimes drives riverine δ^7Li to low, rock-like values, whereas the formation of secondary minerals in intermediate W/D regimes drives riverine δ^7Li to high values.

The carbonate Li isotope values of ~16‰ in the Katian (lower-middle *P. pacificus* zone) are accompanied by low $\delta^{13}C_{org}$ values (stage 1, Fig. 4), corresponding to the late

Boda warming within the *P. pacificus* zone (Fig. 2; Melchin et al., 2013; Myrow et al., 2019; Wang et al., 2023). These relatively high δ^7Li_{carb} values likely reflect more incongruent weathering (i.e. higher W/D), in contrast to several previously analysed global warming events with negative δ^7Li excursions (e.g., OAE 2, Pogge von Strandmann et al., 2013; PETM, Pogge von Strandmann et al., 2021). However, a similar positive δ^7Li excursion accompanying climate warming was observed for the Middle Eocene Climatic Optimum (MECO), albeit with higher absolute δ^7Li values (δ^7Li_{carb} ~22-26‰, Krause et al., 2023) than those in the Late Ordovician. Those authors further proposed that the increased δ^7Li values could be attributed to a shift from a regime with secondary mineral dissolution, to an incongruent weathering regime with secondary mineral formation. Therefore, we suggest that the Katian (lower-middle *P. pacificus* zone) was characterised by more incongruent weathering and higher weathering intensity. The high chemical weathering intensity (high W/D ratios) are supported by local weathering proxies (high CIA) in several sections from South China and Scotland (Yan et al., 2010; Zou et al., 2018; Pogge von Strandmann et al., 2017a). These high CIA values and high W/D ratios are accompanied by high δ^7Li_{carb} values of ~16‰ in the Wuke section and warming climates in the lower and middle parts of the *P. pacificus* zone, suggesting an incongruent weathering regime similar to the MECO (Krause et al., 2023). In such a regime, the supply rate of fresh rocks is likely lower than the weathering rate, leading to extensive clay formation and thick soils. We hence propose that an increase in global volcanic activity in the lower *P. pacificus* zone (Wang et al., 2023) could have initiated the warming event (Boda warming), with the increased terrestrial clay formation due to incongruent weathering leading to more retention of calcium and magnesium in clays, thereby setting a limit on marine carbonate formation and the ocean carbon sink, which could have helped maintain the warm climate (Krause et al., 2023).

Two robust negative δ^7Li_{carb} excursions are recorded during the latest Katian (stage 2) and the latest Hirnantian (stage 4) periods (Fig. 6A), while we attribute the anomalously low δ^7Li_{carb} values in four samples from the early Hirnantian to meteoric diagenesis (Section 5.1). Episodes of enhanced continental weathering due to warm and

humid climates could be expected to generate low seawater δ^7Li values by increasing riverine Li fluxes and driving riverine d^{7}Li values low (Pogge von Strandmann et al., 2017a; Pogge von Strandmann et al., 2021; Sproson et al., 2022). Sea surface temperature reconstructions from the OST indicate a warming climate in the late Katian (lower to middle *P. pacificus* zone), and latest Hirnantian periods (Finnegan et al., 2011; Melchin et al., 2013; Zhang et al., 2021) (Fig. 6C). However, the negative δ^7Li excursion of ~ 4‰ in the latest Katian (upper *P. pacificus* zone) corresponds to increased δ^{13}C values (Fig. 4), and likely coincided with the initiation of cooling or glaciation (Fig. 6). Hence, in this case, while a transition from incongruent weathering to more congruent weathering was the likely driver for the decreasing δ^7Li values, it appears to have coincided with a cooler climate.

Such a transition to congruent weathering in the latest Katian could potentially have been caused by active tectonism and orogenesis, which could increase the erosion rate and decrease the weathering intensity (W/D). During the amalgamation of the Peri-Gondwanan terrane in the Early Paleozoic, the subduction-collision orogenies in the Late Ordovician led to widely distributed volcanic ash deposition (Yang et al., 2019). These Late Ordovician orogenies have been reported in many global settings, such as the Kwangsian Orogeny in South China (Wang et al., 2010; Xu et al., 2016), the Caledonian Orogeny in Scotland (Finlay et al., 2010), and the Taconic Orogeny on the Appalachian margin of Laurentia (van Staal and Barr, 2012). However, tectonic events generally cause a long-term change in continental weathering over several million years, such as the strong tectonism and cooling climate in the late Cretaceous (duration ~ 20 Myr; Jagoutz et al., 2016), early Eocene (~ 16 Myr; Jagoutz et al., 2016) and late Cenozoic (~ 5 Myr; Wan et al., 2012). In addition, previous studies have shown that tectonic uplift and associated changes in silicate weathering took place in the Middle Ordovician, rather than during the Katian (Young et al., 2009; Swanson-Hysell and Macdonald, 2017; Conwell et al., 2022). Therefore, we suggest that orogenesis was not the driver of the congruent weathering in the latest Katian.

We instead suggest that the low δ^7Li values in the latest Katian (stage 2) could result from enhanced weathering following intense volcanism (Lefebvre et al., 2010). In this

hypothesis, large amounts of volcanic rocks from mantle sources (Yang et al., 2019) were erupted in the late Katian (stage 1, lower-middle *P. pacificus* zone), with voluminous volcanic CO_2 degassing (low $\delta^{13}C$ values; Fig. 2) and the supply of unradiogenic $^{187}Os/^{188}Os$ (low $^{187}Os/^{188}Os$ ratios, Finlay et al., 2010; Fig. 6B). However, high weathering rates under a warming climate apparently exceeded the supply rate of fresh rocks in this interval, which would have led to a high chemical weathering intensity, as discussed above (i.e. higher δ^7Li and W/D values). Subsequently, the origin of the parental magma is suggested to have changed from a depleted mantle source to a crustal source during the OST (Yang et al., 2019), contributing to the enhanced weathering of the felsic fresh rocks and increasing $^{187}Os/^{188}Os$ ratios (Finlay et al., 2010; Fig. 6B) in the latest Katian. Alternatively, volcanism emitted the CO_2 to increase temperature and weathering, and that the main rock type being weathered was still acidic. So the weathering of new mafic rocks in stage 1 was overshadowed by increased weathering of all the continental rocks that were already there. Overall, both the enhanced weathering of felsic fresh rocks and continental rocks, with rate of fresh rocks supply exceeding weathering rate, could have accelerated the congruent weathering (i.e., lower δ^7Li and W/D values; Fig. 6A), increased atmospheric CO_2 consumption, and led to the initiation of climate cooling in the latest Katian (Lefebvre et al., 2010). Such a scenario of volcanism-induced early warming and late cooling within a few million years has been widely proposed for other geological intervals, such as the Cryogenian (Lu et al., 2022), the Permo-Carboniferous transition (Yang et al., 2018), and the late Permian (Yang et al., 2020).

The negative δ^7Li excursion in the latest Hirnantian period was larger (~ 6‰) and coincided with warming (stage 4, Fig. 6A) which is consistent with a warming-driven increase in rainfall frequency and intensity, as suggested for the Early Triassic, Cretaceous, and Paleocene-Eocene Thermal Maximum (Pogge von Strandmann et al., 2013, 2021; Lechler et al., 2015; Cao et al., 2022). There was also a marked increase in siliciclastic supply (e.g. quartz, feldspar) from the early Hirnantian to the latest Hirnantian, which was recorded in the lower Butuo Formation from the shallow shelf (Fig. 4). Enhanced siliciclastic supply was also seen in the lower Silurian shales of the

lower Longmaxi Formation from the deep-shelf of the Yangtze Platform (Zou et al., 2018). In addition, the latest Hirnantian is widely regarded as a time of significant glacial retreat, which is supported by the persistence of smaller ice sheets in North Africa and Libya (Moreau, 2011; Le Heron et al., 2013). This glacial retreat would have further contributed to the enhanced river runoff and denudation rate. Overall, the lower $\delta^7Li_{seawater}$ values in the latest Hirnantian can be attributed to a relatively greater increase in denudation rates compared to weathering rates (i.e. lower W/D), potentially also accompanied by an increase in total weathering fluxes.

Positive δ^7Li excursions are observed in the Hirnantian glaciation (stage 3, Fig. 6A) and the early Rhuddanian (stage 5, Fig. 6A). As previously proposed, a transition from congruent weathering to more incongruent weathering was likely the driver for the increasing δ^7Li values during the Hirnantian glaciation (Pogge von Strandmann et al., 2017a). During the glaciation, cooling and arid intervals would lead to decreased rainfall, thereby causing a greater decrease in the denudation rate than the weathering rate (i.e. higher W/D). The resulting decreases in continental weathering fluxes during the glaciation are further supported by low seawater $^{187}Os/^{188}Os$ ratios (Finlay et al., 2010). In these periods, thicker soil formation would generate a more incongruent weathering regime with higher W/D ratios and more clay formation, contributing to the increased δ^7Li values (Figs. 4-6). Following the low δ^7Li values accompanying the climate warming and deglaciation of the latest Hirnantian, the δ^7Li values increased again to similarly high values of ~15‰ during the Rhuddanian (Figs. 4-6). Such values could reflect the attenuation of melting ice (Moreau, 2011; Le Heron et al., 2013) and a cooling climate (Yang et al., 2024), which would have reduced river runoff and erosion rates, and increased the chemical weathering intensity (Yang et al., 2023), generating an incongruent weathering regime with higher W/D ratios and higher δ^7Li values in the Rhuddanian.

5.4 Modelling the seawater Li isotope variations

The behaviour of Li and its isotopes across the OST was modelled using dynamic (non-steady state) box models based on previous studies (Pogge von Strandmann et al.

2013, 2017a, 2021; Lechler et al 2015; Sproson et al., 2022). The dynamic mass balance equation for Li is as follows:

$$dN/dt = F_{riv} + F_{hyd} - F_{sed} \quad \text{(Equation 1)}$$

where N is the seawater Li reservoir, t is time, and F_x represent the input (riv = river, hyd = hydrothermal) and output (sed = sediment) fluxes (Fig. 8A).

The isotopic mass balance equation is given by:

$$N*d\delta^7Li_{seawater}/dt = F_{riv}(\delta^7Li_{riv} - \delta^7Li_{seawater}) + F_{hyd}(\delta^7Li_{hyd} - \delta^7Li_{seawater}) - F_{sed}(\delta^7Li_{sed} - \delta^7Li_{seawater}) \quad \text{(Equation 2)}$$

where δ^7Li_x are the Li isotope compositions of the riverine (riv), hydrothermal (hyd), and sediment (sed) fluxes, and the seawater reservoir. The value of δ^7Li_{sed} is given by $\Delta_{seawater\text{-}sed} = \delta^7Li_{seawater} - \delta^7Li_{sed}$ (Huh et al., 1998; Misra and Froelich, 2012). The seawater Li evolution was modelled in 10,000-year time-steps, with its residence time basically determined by the initial reservoir size N (2.74×10^{16} mol), which was set at 0.75× the modern value (Pogge von Strandmann et al., 2017a).

As discussed above, the carbonates in the Wuke section are likely composed of primary calcite, similar to the primary mineralogy in the Anticosti Island sections (Pogge von Strandmann et al., 2017a), so the offset between seawater ($\delta^7Li_{seawater}$) and carbonate (δ^7Li_{carb}) is set as ~ 6.1‰ ($\Delta^7Li_{seawater\text{-}calcite}$ = 6.1 ± 1.3‰; Pogge von Strandmann et al., 2019a). However, particular samples in Wuke (latest Katian and Hirnantian) likely experienced early diagenesis, altering the offset between seawater and carbonate (Section 5.1). Therefore, we base the seawater $\delta^7Li_{seawater}$ changes during the OST on a combination of the δ^7Li_{carb} records in the Wuke and Anticosti Island sections (Fig. 6A). We aimed to model several critical periods of $\delta^7Li_{seawater}$ evolution: late Katian (stage 1, Wuke section, $\delta^7Li_{seawater}$ ~ 21‰), latest Katian (stage 2, Anticosti Island sections, $\delta^7Li_{seawater}$ ~ 16‰), early Hirnantian (stage 3, Anticosti Island sections, $\delta^7Li_{seawater}$ ~ 24‰), latest Hirnantian (stage 4, Wuke and Anticosti Island sections, $\delta^7Li_{seawater}$ ~ 16‰), and Rhuddanian (stage 5, Wuke section, $\delta^7Li_{seawater}$ ~ 21‰). In general, the river and hydrothermal input fluxes could be changed to drive these variations in $\delta^7Li_{seawater}$ values, while the sediment output flux (i.e., the formation of marine authigenic aluminosilicate clays and the alteration of basalt) responds to

variations in seawater Li concentrations. Below we discuss plausible scenarios that could explain the reconstructed $\delta^7Li_{seawater}$ evolution.

A small Li isotope fractionation associated with the marine sediment sink ($\Delta_{seawater-sed}$ = 0-10‰) is required to fit the low Precambrian $\delta^7Li_{seawater}$ values (Kalderon-Asael et al., 2021), in contrast to the large Li isotope fractionation in the modern ocean ($\Delta_{seawater-sed}$ ~ 15‰, Misra and Froelich, 2012). Since reverse weathering likely remained at high rates across the OST (Section 5.2; Kalderon-Asael et al., 2021), a muted $\Delta_{seawater-sed}$ value (~ 5‰) was used in this study. In order to achieve the initial Katian $\delta^7Li_{seawater}$ values of ~ 21‰, the δ^7Li_{riv} value was set to 20‰ (modern δ^7Li_{riv} value for the Yellow River; Pogge von Strandmann et al., 2020).

Temperature could also cause changes in δ^7Li_{riv} values and $\Delta_{seawater-sed}$, thereby also influencing the variations of $\delta^7Li_{seawater}$ values (Pogge von Strandmann et al., 2017b, 2020, 2021). A temperature dependence of −0.15‰/K has been observed for the isotope fractionation during marine clay formation ($\Delta_{seawater-sed}$) (Li and West., 2014). However, for a climate warming of 10 K for 400 kyr ($\Delta_{seawater-sed}$ change from 5‰ to 3.5‰), the $\delta^7Li_{seawater}$ value would only decrease by ~1‰ (Fig. 7A). Lithium isotope fractionation during weathering and reverse weathering have been modelled to give a temperature dependence of −0.25‰/K for seawater Li isotope changes during the Cenozoic (Li and West., 2014). Given the estimated temperature changes during the OST (Fig. 6C), the temperature-dependence during such processes could explain a maximum of ~2‰ change in $\delta^7Li_{seawater}$ values (Fig. 8C). Therefore, the direct effect of temperature on isotope fractionation was not the dominant driver of the Li isotope fluctuations through the OST.

Increasing the hydrothermal Li input by 8× relative to the pre-excursion value for 400 kyr would decrease the $\delta^7Li_{seawater}$ value by 6‰ (Fig. 7B), but this change is unrealistically large. Decreasing the δ^7Li_{riv} value from ~ 20‰ to ~ 10‰ for 400 kyr would only result in a 3‰ negative seawater excursion (Fig. 7C). Similarly, increasing or decreasing the riverine weathering flux could not lead to the observed changes in $\delta^7Li_{seawater}$ values (Fig. 7D). Overall, no reasonable single change in the inputs (hydrothermal flux, δ^7Li_{riv}, or riverine flux) could explain the changes in seawater $\delta^7Li_{seawater}$ values during the OST.

Instead, it is likely that multiple factors changed together in response to the climatic perturbations during the OST, mainly including temperature, riverine Li fluxes and

δ^7Li_{riv} values, with the latter two factors controlled by weathering. In order to reproduce the $\delta^7Li_{seawater}$ results of this study, we present one possible solution in which the riverine Li fluxes and δ^7Li_{riv} values vary together (Fig. 8B-C). Coupling the changes in these parameters seems appropriate since the weathering intensity, riverine Li fluxes, and δ^7Li_{riv} values are closely related in modern rivers (Dellinger et al., 2015; Pogge von Strandmann et al., 2021) (Fig. 8B). In our model, we therefore couple high riverine Li fluxes (3 × relative to modern) and congruent weathering (δ^7Li_{riv} ~ 10‰, based on the average δ^7Li values of shield rivers in the Amazon or the Jinsha River; Dellinger et al., 2015; Ma et al., 2020) for the latest Katian (stage 2) and latest Hirnantian (stage 4) intervals (Fig. 8C). In contrast, low riverine Li fluxes (0.7 × relative to modern) combined with more incongruent weathering (δ^7Li_{riv} ~ 30‰, based on Icelandic rivers; Pogge von Strandmann et al., 2020) are used for the Hirnantian glaciation (stage 3) (Fig. 8C). With those parameters, the modelled $\delta^7Li_{seawater}$ evolution (Fig. 8C) is comparable to the reconstruction (Fig. 6A), although the apparent rapidity of some of the transitions in the records cannot be reproduced in the model due to buffering by the ocean residence time of Li.

5.5 Origin of the Hg anomalies during the Ordovician-Silurian Transition: volcanism or weathering?

Volcanism and large igneous province (LIP) formation have received much attention in recent studies because they could influence the climate, oceanic environment, and mass extinctions (Jones et al., 2017; Bond and Grasby, 2020; Smolarek-Lach et al., 2019; Hu et al., 2020, 2021; Jones et al., 2023). Furthermore, volcanic loading can control Hg concentrations in sediments, such that Hg accumulation in sediments may provide a record of past volcanic events over geological timescales (e.g., Pyle and Mather, 2003).

Organic matter, sulfides, and terrigenous materials are considered to be the main host phases of Hg in Ordovician to Silurian sediments (Shen et al., 2019, 2022; Wang et al., 2023). Therefore, it is important to identify the Hg host phases before evaluating sedimentary Hg anomalies. In the Wuke sediments, organic matter is likely the main

host phase for Hg, as evidenced by a significant positive correlation between TOC contents and Hg concentrations (r=+0.68 for Tiezufeike Formation; r=+0.85 for Butuo Formation; Fig. 9A). Although extremely high Hg concentrations in the Ordovician to Silurian shales of South China have been proposed to reflect enhanced Hg uptake by sulfides under euxinic water conditions (Shen et al., 2019, 2022), the total sulfide (TS) contents are low throughout the Wuke section, and there is no consistent correlation between TS contents and Hg concentrations (r=+0.1, for Tiezufeike Formation; r=+0.68, for Butuo Formation; Fig. 9B). Moreover, the overall negative Ce/Ce* anomalies and heavy nitrogen isotope compositions in the Wuke section suggest the local presence of an oxic water mass (Yang et al., 2021; Liu et al., 2022a), which is inconsistent with the hypothesis of Hg enrichment in euxinic water conditions (Shen et al., 2019, 2022). Hence, the above observations suggest that sulfides are not the dominant host phase for Hg in the Wuke section. We further note that Wuke is a carbonate-dominated section with low terrestrial sediment content (Yang et al., 2021; Liu et al., 2022a). The Al_2O_3 concentrations are low (average: 2.3%) throughout the Wuke section, although there is a positive relationship between Al_2O_3 and Hg concentrations in the studied carbonates (r=+0.57, for Tiezufeike Formation; r=+0.63 for Butuo Formation; Fig. 9C), suggesting some importance of clay-bound Hg in the studied sediments.

In general, there is a global lithological control on Hg concentrations in sediments, with limestones showing lower Hg (mean 34.3 μg/kg) concentrations than shales (62.4 μg/kg) (Rudnick and Gao, 2014; Grasby et al., 2019). Given that the Wuke section comprises a mixture of limestones, marls, and shales, we suggest that the Hg/TOC, Hg/Al_2O_3, and Hg/TS ratios are more reliable indicators of changes through time in Hg input from volcanism or weathering than absolute Hg concentrations.

In the lower-middle *P. pacificus* zone (middle to late Katian), Hg/TOC and Hg/Al_2O_3 ratios vary between 1× and 2× baseline values. The mean ratios of both Hg/TOC (~ 90 ppb/%) and Hg/Al_2O_3 (~ 20 ppb/%) in the lower-middle *P. pacificus* zone (stage 1) are higher than those in other Late Ordovician sediments with no volcanic Hg loading (Hg/TOC < 50 ppb/%, Hu et al., 2021; Hg/TOC < 45 ppb/%, Wang et al., 2023; Hg/TOC < 50 ppb/%, Jia et al., 2023), but are comparable to those in Late Ordovician

sediments with volcanic Hg loading (Hg/TOC > 80 ppb/%, Wang et al., 2023; Jia et al., 2023). Several lines of evidence support the attribution of these Hg anomalies to intense volcanism at this time. First, the lower-middle *P. pacificus* zone (middle to late Katian) was characterised by low $\delta^{13}C$ values that have been attributed to the volcanic degassing of more than 1.1×10^{13} tons of ^{12}C-enriched CO_2 in South China (Wang et al., 2023). Second, the distribution of bentonites (volcanic ash) in Late Ordovician sections of the Yangtze Platform provides evidence for the intensity of the volcanism (Su et al., 2009; Ge et al., 2018; Hu et al., 2020, 2021; Yang et al., 2019, 2022; Wang et al., 2023; Jia et al., 2023), with a general trend towards thinner bentonites from the middle to the upper Katian implying a gradual diminution of volcanic activity through time (Yang et al., 2022; Jia et al., 2023). Third, the eroded and deformed remnants of a possible LIP have been observed in northern Iran in the late Katian, supporting volcanism in this region in the late Ordovician (Derakhshi et al., 2022). Fourth, geochemical ratios (e.g., Cr/Al_2O_3, V/Al_2O_3, Zr/Cr, and Zr/Al_2O_3; Hu et al., 2021; Yang et al., 2022; Wang et al., 2023) and/or isotope signatures (e.g., $\delta^{13}C_{org}$, $\delta^{34}S_{py}$, $\Delta^{199}Hg$, and $\Delta^{33}S$; Hu et al., 2020; Li et al., 2021a) indicate intense volcanic activity in the lower-middle *P. pacificus* zone (Yang et al., 2022; Jia et al., 2023), although the positive $\Delta^{199}Hg$ values in deep-water shelf settings are likely related to long-distance transport of volcanogenic Hg (Gong et al., 2017; Shen et al., 2022b). The magma sources during this period are proposed to have been derived from the mantle (Yang et al., 2019), which is supported by an unradiogenic seawater $^{187}Os/^{188}Os$ excursion (Finlay et al., 2010, Fig. 6B). Therefore, we consider that volcanic Hg contributed to the intermediate Hg/TOC and Hg/Al_2O_3 ratios in the late Katian (lower-middle *P. pacificus*) of the Wuke section (Figs. 4 and 6F).

The latest Katian (stage 2, upper *P. pacificus*) is also characterised by high Hg/TOC ratios relative to those in the Hirnantian and Rhuddanian (Fig. 4). Notably, two Hg peaks in the latest Katian are seen when the Hg concentration is normalised to any of TOC, TS, or Al_2O_3 (> 2× baseline value), with high Hg/TOC ratios recorded in two samples for each peak (Fig. 4). We note that the latest Katian interval corresponds to an increase in $\delta^{13}C_{org}$ values (from -29‰ to -28‰) (Fig. 4), which is inconsistent with

the degassing of ^{12}C-depleted CO_2 by volcanism. Generally, soils and vegetation (1200 × 10^6 mol Hg) are the most important reservoirs of Hg in the earth surface system (Zhang et al., 2014), with the Hg in soils mainly being delivered to the ocean by riverine particles such as clays (Kongchum et al., 2011). Since rivers represent the largest source of Hg to the global coastal oceans (5×10^6 mol y^{-1}; 76% of the new Hg supplied into coastal oceans; Liu et al., 2021a), an increase in riverine sediment fluxes would increase the global Hg burial in continental shelf sediments (Liu et al., 2021a). Given the proposed increase in weathering and denudation rates during the latest Katian (Fig. 6), an increase in riverine Hg fluxes to the ocean could be expected. However, it unlikely to have driven the increases in Hg/TOC and Hg/Al_2O_3 ratios because the rivers would also have delivered large amounts of organic matter and clays. In the latest Katian, the elevated Hg/TOC and Hg/Al_2O_3 ratios coincided with a decrease in δ^7Li values (Fig. 6A, F). Therefore, we speculate that the more congruent weathering was associated with enhanced dissolution of primary rocks such as basalts, which would have released a large amount of Hg into soils (Gao et al., 2023), and hence onto particles (e.g. organic matter, clays, Fe-Mn oxides) to be transported by rivers to the ocean. Previous studies suggested that the Hg anomalies in the latest Katian were related to volcanic-induced Hg loading, as recorded in deep ocean settings (USA, > 1000 ppb/%, Jones et al., 2017, Hu et al., 2021; Poland, > 500 ppb/%, Smolarek-Lach et al., 2019). However, the volcanogenic source of Hg in the latest Katian of South China has been challenged in recent studies due to slightly high $\Delta^{199}Hg$ values (Shen et al., 2019, 2022; Liu et al., 2023b; Zhou et al., 2024). Variable $\Delta^{199}Hg$ values on the Yangtze Platform suggest different Hg sources were important in different settings, with deep-water shelf sites showing higher values, representing seawater-sourced Hg (Shen et al., 2019, 2022; Liu et al., 2023b), and shallow-water shelf sites showing lower values, representing a significant regional terrigenous Hg flux (Liu et al., 2023b). Notably, high Hg/TOC and Hg/Al_2O_3 ratios induced by enhanced weathering have previously been proposed for the mid-Proterozoic (up to ~200 ppb/% for Hg/TOC, Tang et al., 2022) and the Ediacaran–Cambrian boundary (up to ~10000 ppb/% for Hg/TOC, Liu et al., 2021b). Here we suggest that the enhanced dissolution of primary rocks under congruent

weathering conditions (Fig. 6A), and the increased erosion of soil minerals, could also have led to an enhanced delivery of riverine Hg into the ocean and increased Hg burial on the shallow shelf during the latest Katian (Fig. 6F).

The Hirnantian and Rhuddanian are characterised by overall low Hg/TOC ratios, representing the background values of weak or no volcanism in the Early Silurian (Zhou et al., 2024). Volcanic ash is rare in the Hirnantian and lower Rhuddanian and is prevalent throughout the upper part of the Rhuddanian, indicating that the intensity of volcanism was weak in the latest Hirnantian, and then became stronger into the upper part of the Rhuddanian (Yang et al., 2019; Qiu et al., 2022; Shen et al., 2022a; Liu et al., 2023b). The samples in the latest Hirnantian show high Hg/Al_2O_3 ratios (exceeding 2 × baseline) but do not have elevated Hg/TOC ratios (between 0.5 × to 2 × baseline) (Fig. 4), so this Hg may have been associated with the elevated TOC levels. Therefore, no obvious sedimentary Hg anomalies can be demonstrated in our data for the latest Hirnantian of the Wuke section, although extremely high Hg/TOC ratios have been observed in other regions (Smolarek-Lach et al., 2019; Bond and Grasby, 2020; Sial et al., 2024; Fig. 6). Overall, more detailed research is needed to evaluate the possible contributions of weathering to Hg fluxes in the latest Hirnantian.

5.6 Implications for global climate and the Late Ordovician Mass Extinctions

Global cooling in the Hirnantian has been proposed based on the occurrence of sediments deposited by glaciers, and isotope analysis of carbonates and fossils (Finnegan, et al., 2011). The apparent decline in atmospheric CO_2 and climatic cooling have been attributed to various mechanisms, including enhanced burial of organic carbon, enhanced silicate weathering, and reduced volcanic outgassing (Finlay et al., 2010; Lefebvre et al., 2010; Lenton et al., 2012; Pogge von Strandmann et al., 2017a; Sproson et al., 2022). The evolution of $\delta^7Li_{seawater}$ during the OST helps us to understand the relationship between climate and chemical weathering (Fig. 6; Pogge von Strandmann et al., 2017a, 2021a; Sproson et al., 2022).

The late Katian (lower-middle *P. pacificus* zone) was characterised by intense volcanism and incongruent weathering (Fig. 6; stage 1; high $\delta^7Li_{seawater}$ values and low

$^{187}Os/^{188}Os$ and $\delta^{13}C$ values), potentially pointing to a role for volcanic activity in initiating the late Boda warming. The enhanced secondary mineral formation could have helped sustain the warm climate because clay formation reduces the flux of carbonate-forming cations and nutrient cations to the oceans (Krause et al., 2023). Intervals of enhanced and congruent weathering (Fig. 6; low $\delta^7Li_{seawater}$ values and high $^{187}Os/^{188}Os$ and $\delta^{13}C_{org}$ values) occurred in both the latest Katian (stage 2; upper *P. pacificus* zone) and latest Hirnantian (stage 4; upper *M. persculptus* zone). Given that the onset of the decrease in $\delta^7Li_{seawater}$ values in the latest Katian coincided with the initial increase in $\delta^{13}C_{org}$ (Fig. 4), it is feasible that enhanced continental weathering in the Late Ordovician (Finlay et al., 2010; Lefebvre et al., 2010; Swanson-Hysell and Macdonald, 2017; Conwell et al., 2022) lowered atmospheric CO_2 over this timescale and cooled the climate, potentially even triggering the Hirnantian glaciation. During the Hirnantian glaciation itself, decreased and incongruent weathering (Fig. 6; stage 3; high $\delta^7Li_{seawater}$ values and low $^{187}Os/^{188}Os$ ratios) during the glacial intervals could have contributed to reduced CO_2 drawdown, ultimately allowing climatic recovery. The congruent weathering in the latest Hirnantian (Fig. 6A; stage 4) was likely caused by the increased precipitation and runoff under a warming climate following deglaciation, and probably also enhanced by rapid weathering of fine-grained glacial till. The enhanced weathering could then have reduced the atmospheric CO_2 and generated another cooling event, but such cooling was apparently limited by the more incongruent weathering in the Rhuddanian (Fig. 6A; stage 5; return to high $\delta^7Li_{seawater}$ values). Overall, our new record suggests that continental weathering may be capable of eventually stabilising climate when the climatic system is out of balance, but was not a sufficiently fast process to prevent significant climate fluctuations during the OST.

Traditionally, the LOME was considered to comprise two phases in the Late Ordovician (Harper et al., 2014), with the first phase (LOME 1) corresponding to the start of the Hirnantian glaciation, and the second phase (LOME 2) occurring in the latest Hirnantian (Harper et al., 2014). However, as shown by recent studies (Deng et al., 2021; Harper, 2024), the initial biodiversity decline in fact occurred within the middle-late Katian (Katian extinction, or LOME 0; Fig. 6E). Several hypotheses have been

proposed for the causes of these extinctions, such as volcanism, ocean euxinia, and climate change (Fig. 6, Harper et al., 2014; Jones et al., 2017; Zou et al., 2018; Hu et al., 2020; Lu et al., 2024). The new records of $\delta^7Li_{seawater}$ values and Hg concentrations, together with existing thallium (Tl) and uranium (U) isotope records (Kozik et al., 2022a; Liu et al., 2022a), could provide further insights into the triggering mechanisms for the LOME (Fig. 6).

The variations of U and Tl isotopes imply that there was a rapid global expansion of oxygen minimum zones in both the Katian and the latest Hirnantian, interrupted by a rapid contraction of these oxygen minimum zones during the Hirnantian cooling events (Fig. 6D; Liu et al., 2022a; Kozik et al., 2022a; Lu et al., 2024). However, the late Katian (lower-middle *P. pacificus* zone) was characterised by decreased and incongruent weathering, which raises the question of what drove the initial expansion of anoxia during this period. Given the lack of evidence for elevated weathering, and the relatively high Hg/TOC ratios (Figs. 4 and 6), our data support the view that an increased input of nutrients from globally increased volcanism led to the high primary productivity (Longman et al., 2021) and helped drive anoxia. This ocean anoxia could then contribute to the Katian extinction (Fig. 6; Lu et al., 2024; Chen et al., 2024). Subsequently, the anoxia and occasionally euxinic conditions could have led to the LOME 1 in the latest Katian and the LOME 2 in the latest Hirnantian (Fig. 6; Zou et al., 2018; Harper, 2024).

An interesting observation here is the similarity of the Li isotope and U isotope records (Liu et al., 2022a) in the Wuke section, with low $d^7Li_{seawater}$ values and low $d^{238}U_{carb}$ values likely indicating a close relationship between continental weathering and expanded euxinic seawaters in the latest Katian and latest Hirnantian (Fig. 6A, D). Generally, U inputs to the modern ocean are dominated by rivers (Andersen et al., 2016, 2017), with an average $\delta^{238}U$ value for global rivers that is indistinguishable from that of the upper continental crust (Tissot and Dauphas, 2015). Euxinic, ferruginous, and suboxic sediments are the main sinks for U, with the ferruginous or euxinic conditions showing significantly higher $\delta^{238}U$ values than seawater ($\Delta^{238}U_{seawater\text{-}anoxic\ sediments}$ ~ 0.7‰, $\Delta^{238}U_{seawater\text{-}euxinic\ sediments}$ ~ 0.6-0.8‰, Andersen et al., 2017). Therefore, seawater

$\delta^{238}U$ reconstructions are widely used to evaluate seawater anoxia, with lower $\delta^{238}U$ values indicating more reducing water conditions (e.g. Liu et al., 2022a; Lu et al., 2024). In the latest Katian and latest Hirnantian intervals, enhanced and congruent weathering would have increased the riverine sulfate inputs and the supply of dissolved nutrients to the ocean, with the sulfate inputs providing a source for sulfate reduction and thereby contributing to the expansion of euxinic seawater (Li et al., 2021b). Such changes could therefore explain the observed link between the Li and U isotope records (Fig. 6). In addition, the changes in riverine U fluxes could also affect the oceanic U cycle, which may further influence the calculation of redox conditions in the global ocean. Since the reconstructed $\delta^{7}Li_{seawater}$ values suggest that the weathering flux was likely variable during the OST, quantitative estimates of changes in the extent of euxinic/anoxic bottom waters during the OST based on the $\delta^{238}U_{carb}$ data might be re-estimated (Fig. 6; Liu et al., 2022a). However, an enhanced riverine input of U could not on its own explain the low $\delta^{238}U_{carb}$ values reached during these excursions (Fig. 6D). Overall, the enhanced nutrient inputs point to the potential role of weathering in inducing high primary productivity and driving further expansion of ocean anoxia and euxinia. Such anoxic and euxinic conditions could then have driven the extinctions during the LOME 1 and LOME 2 events (Fig. 6).

6. Conclusions

New records of Li isotopes and Hg concentrations in a carbonate section from South China were used to track the relationship between climate, volcanism, and continental weathering during the OST. The carbonate Li isotope compositions were variable across the OST, with several distinct intervals of $\delta^{7}Li_{seawater}$ evolution being inferred (late Katian: ~ 21‰, latest Katian: ~ 16‰, Hirnantian: ~ 24‰, latest Hirnantian: ~ 16‰, and Rhuddanian: ~ 21‰). The variations of $\delta^{7}Li_{seawater}$ could be explained predominantly by changes in dissolved riverine Li fluxes and $\delta^{7}Li_{riv}$ values caused by changes in continental weathering, with some influence also from changes in temperature. Meanwhile, high Hg/TOC and Hg/Al_2O_3 ratios occurred during the Late Katian, enabling intervals of volcanic activity or weathering-induced Hg input to be

identified.

The records provide evidence for variable continental weathering regimes and fluxes responding to, and potentially influencing, the climatic fluctuations of the OST. An increase in volcanic activity (high Hg/TOC and low $\delta^{13}C_{org}$ values) likely initiated the warming climate (late Boda warming event) in the Late Katian, which was sustained by enhanced clay formation (high $\delta^{7}Li_{seawater}$ values). Extremely enhanced and more congruent weathering (low $\delta^{7}Li_{seawater}$ values) would have lowered atmospheric CO_2 in the latest Katian and contributed to global cooling. In contrast, decreased and incongruent weathering (high $\delta^{7}Li_{seawater}$ values) during Hirnantian glacial intervals could have contributed to reduced CO_2 drawdown, ultimately allowing climatic recovery.

The multi-phase biotic extinctions in the Late Ordovician can be attributed to a combination of volcanism-induced and/or weathering-induced oceanic anoxia. Intense volcanism, rather than continental weathering changes, appears to have contributed to the high primary productivity and expansion of anoxia during the Katian extinction (LOME 0). However, enhanced and congruent weathering probably played a more important role in driving the expansion of euxinic seawater in the latest Katian and latest Hirnantian intervals, thereby contributing to the Late Ordovician Mass Extinction (LOME 1 and LOME 2) events.

Acknowledgements

The work presented in this paper was supported by the Natural Science Foundation of China (42402123, 41690131), the Natural Science Foundation of Hubei Province (2019CFA028), and the Fundamental Research Funds for National Universities, China University of Geosciences (Wuhan). Philip Pogge von Strandmann is funded by ERC grant 682760 (CONTROLPASTO2). David Wilson is funded by a Natural Environment Research Council independent research fellowship (NE/T011440/1). Xiangrong Yang gratefully acknowledges financial support from the China Scholarship Council, and thanks Gary Tarbuck, Susan Little, Kun Zhang, and Xi Chen for their help. We are also grateful to three anonymous reviewers for their thoughtful comments that

helped us to improve the manuscript. For the purpose of open access, the author has applied a 'Creative Commons Attribution (CC BY) licence' to any Author Accepted Manuscript version arising.

CRediT authorship contribution statement

Xiangrong Yang: Data curation, Formal analysis, Methodology, Writing – original draft, Writing – review & editing. **Detian Yan**: Funding acquisition, Investigation, Writing – review & editing. **David J. Wilson**: Funding acquisition, Methodology, Writing – review & editing. **Philip A. E. Pogge von Strandmann**: Funding acquisition, Methodology, Writing – review & editing. **Xianyi Liu**: Methodology, review & editing. **Chun-Yao Liu**: Methodology, Writing – review & editing. **Mu Liu**: Writing – review & editing. **Liwei Zhang**: Writing – review & editing. **Bao Zhang**: Writing – review & editing. **Daizhao Chen**: Writing – review & editing.

References

Andersen, M.B., Vance, D., Morford, J.L., Bura-Naki´c, E., Breitenbach, S.F.M., Och, L., 2016. Closing in on the marine $^{238}U/^{235}U$ budget. Chemical Geology, 420, 11–22.

Andersen, M.B., Stirling, C.H., Weyer, S., 2017. Uranium Isotope Fractionation. Reviews in Mineralogy & Geochemistry, 82, 799–850.

Berner, R. A., 1992. Weathering, plants, and the long-term carbon cycle. Geochimica et Cosmochimica Acta, 56, 3225–3231.

Berner, R.A., Lasaga, A.C., Garrels, R.M., 1983. The Carbonate-Silicate Geochemical Cycle and Its Effect on Atmospheric Carbon Dioxide over the Past 100 Million Years. American Journal of Science, 283, 641–683.

Bond, D.P.G., Grasby, S.E., 2020. Late Ordovician mass extinction caused by volcanism, warming, and anoxia, not cooling and glaciation. Geology, 48, 777–781.

Buggisch, W., Michael, M., Joachimski., Lehnert, O., Bergstroem, S.M., Repetski, J.E., Webers, G.F., 2010. Did intense volcanism trigger the first Late Ordovician

icehouse? Geology, 38(4), 327–330.

Cao, C., Bataille, C.P., Song, H.J., Saltzman, M.R., Cramer, K. T., Wu, H.C., Korte, C., Zhang, Z.F., Liu, X.M., 2022. Persistent late permian to early triassic warmth linked to enhanced reverse weathering. Nature Geoscience, 15(12), 1071–1071.

Chen, X., Rong, J.Y., Li, Y., Boucot, A.J., 2004. Facies patterns and geography of the Yangtze region, South China, through the Ordovician and Silurian transition. Palaeogeography, Palaeoclimatology, Palaeoecology, 204, 353–372.

Chen, X.M., Romaniello, S.J., Herrmann, A.D., Hardisty, D., Gill, B.C., Anbar, A.D., 2018. Diagenetic effects on uranium isotope fractionation in carbonate sediments from the Bahamas. Geochimica et Cosmochimica Acta, 237(15), 2943–311.

Chen, C., Wang, J.S., Thomas, T. J., Chen, X. H., Wang, Z., Tu, S., Wang, G.Z., Yang, J.X., 2017. Negative $\delta^{13}C_{carb}$ shifts in Upper Ordovician (Hirnantian) Guanyinqiao Bed of South China linked to diagenetic carbon fluxes. Palaeogeography, Palaeoclimatology, Palaeoecology, 487, 430–446.

Chen, C., Wang, J.S., Thomas, T. J., Chen, X. H., Wang, Z., Ma, X.C., Cen, Y., Zhao, J., 2020. New evidence for compaction-driven vertical fluid migration into the Upper Ordovician (Hirnantian) Guanyinqiao bed of south China. Palaeogeography, Palaeoclimatology, Palaeoecology, 550, 109746.

Chen, C., Wang, J.S., Chen, X.H., Algeo, T.J., Wang, Z., Yang, W. W., Song, Q., 2024. Productivity and redox influences on the late Ordovician 'Katian Extinction' and 'early Silurian Recovery'. Palaeogeography, Palaeoclimatology, Palaeoecology, 642, 112176.

Conwell, C.T., Saltzman, M.R., Edwards, C.T., Griffith, E.M., Adiatma, Y.D., 2022. Nd isotopic evidence for enhanced mafic weathering leading to Ordovician cooling. Geology, 50, 886–890.

Day, C.C., Pogge von Strandmann, P.A.E., Mason, A.J., 2021. Lithium isotopes and partition coefficients in inorganic carbonates: Proxy calibration for weathering reconstruction. Geochimica et Cosmochimica Acta, 305, 243–262.

Dellinger, M., Gaillardet, J., Bouchez, J., Calmels, D., Louvat, P., Dosseto, A., Gorge, C., Alanoca, L., Maurice, L., 2015, Riverine Li isotope fractionation in the

Amazon River basin controlled by the weathering regimes. Geochimica et Cosmochimica Acta, 164, 71–93.

Dellinger, M., Hardisty, D.S., Planavsky, N.J., Gill, B.C., Kalderon-Asael, B., Asael, D., Croissant, T., Swart, P.K., West, A. J. 2020. The effects of diagenesis on lithium isotope ratios of shallow marine carbonates. American Journal of Science, 320, 150–184.

Deng, K., Yang, S.Y., Guo, Y.L., 2022. A global temperature control of silicate weathering intensity. Nature Communications, 13, 1781.

Deng, Y., Fan, J.X., Zhang, S.H., Fang, X., Chen, Z.Y., Shi, T.K., Wang, H.W., Wang, X.B., Yang, J., Hou, X.D., 2021, Timing and patterns of the Great Ordovician Biodiversification Event and Late Ordovician mass extinction: Perspectives from South China. Earth-Science Reviews, 220, 103743.

Derakhshi, M., Ernst, R.E., Kamo, S.L., 2022. Ordovician-Silurian volcanism in northern Iran: Implications for a new Large Igneous Province (LIP) and a robust candidate for the Late Ordovician mass extinction. Gondwana Research, 107, 256–280.

Dunlea, A.G., Murray, R.W., Ramos, D.P.S., Higgins, J.A., 2017. Cenozoic global cooling and increased seawater Mg/Ca via reduced reverse weathering. Nature Communications, 8, 844.

Fan, J.X., Shen, S., Erwin, D.H., Sadler, P.M., MacLeaod, N., Cheng, Q., Hou, X., Yang, J., Wang, X., Wang, Y., Zhang, H., Chen, X., Li, G., Zhang, Y., Shi, Y., Yuan, D., Chen, Q., Zhang, L., Li, C., Zhao, Y., 2020. A high-resolution summary of Cambrian to early Triassic marine invertebrate biodiversity. Science, 367, 272–277.

Finlay, A.J., Selby, D., Gröcke, D.R., 2010. Tracking the Hirnantian glaciation using Os isotopes. Earth and Planetary Science Letters, 293, 339–348.

Finnegan, S., Bergmann, K., Eiler, J.M., Jones, D.S., Fike, D.A., Eisenman, I., Hughes, N.C., Tripati A.K., Fischer, W.W., 2011, The magnitude and duration of Late Ordovician-Early Silurian glaciation. Science, 331, 903–906.

Flesch, G.D., Anderson, A.R., Svec, H.J.A., 1973. Secondary isotopic standard for

$^{6}Li/^{7}Li$ determinations. International Journal Mass Spectrometry and Ion Processes, 12, 265–272.

Gao, X., Yuan, W., Chen, J.B., Huang, F., Wang, Z.R., Gong, T.F., Zhang, Y.M., Liu, Y., Zhang, T., Zheng, W., 2023. Tracing the source and transport of Hg during pedogenesis in strongly weathered tropical soil using Hg isotopes. Geochimica et Cosmochimica Acta, 361, 101-112.

Ge, X.Y., Mou, C.L., Wang, C.S., Men, X., Chen, C., Hou, Q., 2018. Mineralogical and geochemical characteristics of K-bentonites from the Late Ordovician to the Early Silurian in South China and their geological significance. Geological Journal, 1–15.

Gernon, T.M., Hincks, T.K., Merdith, A.S., Rohling, E.J., Palmer, M.R., Foster, G.L., Bataille, C. P., Müller, R.D. Global chemical weathering dominated by continental arcs since the mid-Palaeozoic. 14, 690-696.

Gong, Q., Wang, X., Zhao, L., Grasby, S.E., Chen, Z.Q., Zhang, L., Li, Y., Cao, L., Li, Z., 2017, Mercury spikes suggest volcanic driver of the Ordovician-Silurian mass extinction: Scientific Reports, 7, 5304.

Grasby, S.E., Themm II, T.R., Chen, Z.H., Yin, R.S., Ardakani, O.H., 2019. Mercury as a proxy for volcanic emissions in the geologic record. Earth-Science Reviews, 196, 102880.

Harper, D.A.T., 2024. Late Ordovician Mass Extinction: Earth, fire and ice. National Science Review, 11, nwad319.

Harper, D.A.T., Hammarlund, E.U., Rasmussen, C. M. O., 2014. End Ordovician extinctions: A coincidence of causes. Gondwana Research, 25, 1294–1307.

Hathorne, E.C., James, R.H., 2006. Temporal record of lithium in seawater: A tracer for silicate weathering? Earth and Planetary Science Letters, 246, 393–406.

Higgins, J.A., Blättler, C.L., Lundstrom, E.A., Santiago-Ramos, D.P., Akhtar, A.A., Ahm, A.S.C., Bialik, O., Holmden, C., Bradbury, H., Murray, S.T., Swart, P.K., 2018. Mineralogy, early marine diagenesis, and the chemistry of shallow-water carbonate sediments. Geochimica et Cosmochimica Acta, 220, 512–534.

Huh, Y., Chan, L.H., Zhang, L., Edmond, J.M., 1998. Lithium and its isotopes in major

world rivers: Implications for weathering and the oceanic budget. Geochimica et Cosmochimica Acta, 62(12), 2039–2051.

Hu, D.P., Li, M.H., Chen, J.B., Luo, Q.Y., Grasby, S.E., Zhang, T.G., Yuan, S.L., Xu, Y.L., Finney, S.C., Sun, L.L., Shen, Y.N., 2021. Major volcanic eruptions linked to the Late Ordovician mass extinction: Evidence from mercury enrichment and Hg isotopes. Global and Planetary Change, 196, 103374.

Hu, D.P., Li, M.H., Zhang, X.L., Turchyn, A.V., Gong, Y.Z., Shen, Y.A., 2020. Large mass independent sulphur isotope anomalies link stratospheric volcanism to the Late Ordovician mass extinction. Nature Communication, 11(1), 2297.

Hu, D.P., Zhang, X. L, Zhou, L., Finney, S.C., Liu, Y.S., Shen, D., Shen, M., Huang, W., Shen, Y.N., 2017. $^{87}Sr/^{86}Sr$ evidence from the epeiric Martin Ridge Basin for enhanced carbonate weathering during the Hirnantian. Scientific Reports, 7, 11348.

Isson, T.T., Planavsky, N.J., 2018. Reverse weathering as a long-term stabilizer of marine pH and planetary climate. Nature, 560, 471–475.

James, N.P., Choquette, P.W., 1984. Diagenesis .9. Limestones-the meteoric diagenetic environment. Geoscience Canada, 11(4), 161–194.

Jagoutz, O., Macdonald, F.A., Royden, L., 2016. Low-latitude arc–continent collision as a driver for global cooling. 113(18), 4935–4940.

Jia, J.X., Du, X.B., Zhao, K., Ma, Z.Y., 2023. Different integrated mechanisms drove the two pulses of the Late Ordovician mass extinction. Palaeogeography, Palaeoclimatology, Palaeoecology, 620, 111572.

Jones, D.S., Brothers, R.W., Crüger Ahm, A.-S., Slater, N., Higgins, J.A., Fike, D.A., 2020. Sea level, carbonate mineralogy, and early diagenesis controlled $\delta^{13}C$ records in Upper Ordovician carbonates. Geology, 48, 194–199.

Jones, D., Martini, A., Fike, D., 2017. A volcanic trigger for the Late Ordovician mass extinction? Mercury data from south China and Laurentia. Geology, 45, 631–634.

Jones, D.S., Fike, D.A., Finnegan, S., Fischer, W.W., Schrag, D.P., McCay, D., 2011. Terminal Ordovician carbon isotope stratigraphy and glacioeustatic sea-level change across Anticosti Island (Québec, Canada), Bulletin of the Geological Society of America, 123, 1645–1664.

Jones, M.T., Stokke, E.W, Rooney, A.D, Frieling, J, von Strandmann, P.A.E.P, Wilson, D.J, Svensen, H.H , Planke, S, Adatte, T, Thibault, N, Vickers, M.L, Mather, T.A, Tegner, C, Zuchuat, V, Schultz, B.P, 2023. Tracing North Atlantic volcanism and seaway connectivity across the Paleocene-Eocene Thermal Maximum (PETM). Climate of the Past, 19(8), 16235–1652.

Kalderon-Asael, B., Katchinoff, J.A.R., Planavsky, N.J., Hood, A. V. S., Dellinger, M., Bellefroid, E. J., Jones, D. S., Hofmann, A., Ossa, F. O., Macdonald, F. A., Wang, C. J., Isson, T. T., Murphy, J. G., Higgins, J. A., West, A. J., Wallace, M. W., Asael, D., Pogge von Strandmann, P. A. E., 2021. A lithium-isotope perspective on the evolution of carbon and silicon cycles. Nature, 595, 394–398.

Kimmig, S.R., Holmden, C., 2017, Multi-proxy geochemical evidence for primary aragonite precipitation in a tropical-shelf 'calcite sea' during the Hirnantian glaciation. Geochimica et Cosmochimica Acta, 206, 254–272.

Kisakurek, B., James, R.H., Harris, N.B.W., 2005. Li and δ^7Li in Himalayan rivers: proxies for silicate weathering? Earth and Planetary Science Letters, 237, 387–401.

Kongchum, M., Hudnall, W.H., Delaune, R., 2011. Relationship between sediment clay minerals and total mercury. Journal of Environmental Science and Health Part A, 46 (5), 534–539.

Kozik, N.P., Young, S.A., Newby, S.M., Liu, M., Chen, D.Z., Hammarlund, E.U., Bond, D.P.G., li, T.R.T., Owens, J.D., 2022a. Rapid marine oxygen variability: Driver of the Late Ordovician mass extinction. Science Advances, 8(46), eabn8345.

Kozik, N.P., Gill, B. C., Owens, J.D., Lyons, T.W., Young, S.A., 2022b. Geochemical records reveal protracted and differential marine redox change associated with Late Ordovician climate and mass Extinctions. AGU Advances, 3(1), e2021AV000563.

Krause, A.J., Sluijs, A., Ploeg, R.V.D., Lenton, T.M., Pogge von Strandmann, P.A.E., 2023. Enhanced clay formation key in sustaining the Middle Eocene Climatic Optimum. Nature Geoscience, 16, 730–738.

Kump, L.R., Arthur, M.A., 1999. Interpreting carbon – isotope excursions: carbonates

and organic matter. Chemical Geology, 161 (1), 181–198.

Lechler, M., Pogge von Strandmann, P.A.E., Jenkyns, H.C., Prosser, G., Parente, M., 2015. Lithium-isotope evidence for enhanced silicate weathering during OAE 1a (Early Aptian Selli event). Earth and Planetary Science Letters, 432, 210–222.

Lefebvre, V., Servais, T., Francois, L., Averbuch, O., 2010. Did a Katian large igneous province trigger the Late Ordovician glaciation?: A hypothesis tested with a carbon cycle model. Palaeogeography Palaeoclimatology Palaeoecology, 296, 310–319.

Le Heron, D.P., and Dowdeswell, J.A., 2009. Calculatingice volumes and ice flux to constrain the dimensionsof a 440 Ma North African ice sheet: Journal of theGeological Society of London, 166, 277–281.

Lenton, T., Michael, C., Martin J., Pires, N., Dolan, L., 2012. First plants cooled the Ordovician. Nature Geoscience, 5, 86–89.

Li, Y.F., Zhang, T.W., Shen, B.J., Li, Z.M., Shao, D.Y., Lash, G.G., 2021a. Carbon and sulfur isotope variations through the Upper Ordovician and Lower Silurian of South China linked to volcanism. Palaeogeography, Palaeoclimatology, Palaeoecology, 567, 110285.

Li, N., Li, C., Algeo, T.J., Cheng, M., Jin, C.S., Zhu, G.Y., Fan, J.X., Sun, Z.Y., 2021b. Redox changes in the outer Yangtze Sea (South China) through the Hirnantian Glaciation and their implications for the end-Ordovician biocrisis. Earth-Science Reviews, 212, 103443

Li, G.J., West, A.J., 2014. Evolution of Cenozoic seawater lithium isotopes: Coupling of global denudation regime and shifting seawater sinks. Earth and Planetary Science Letters, 401, 284–293.

Liu, M., Chen, D.Z., Jiang, L., Stockey, R.G., Aseal, D., Zhang, B., Liu, K., Yang, X.R., Yan, DT., Planavsky, N.J., 2022a. Oceanic anoxia and extinction in the latest Ordovician. Earth and Planetary Science Letters, 588, 117553.

Liu, M.D., Zhang, Q.R., Maavara, T., Liu, S.D., Wang, X.J., Raymond, P.A., 2021a. Rivers as the largest source of mercury to coastal oceans worldwide. Nature Geosciences, 14, 672–677.

Liu, Z. R. R., Zhou, M. F., Wang, W., 2021b. Mercury anomalies across the Ediacaran–Cambrian boundary: Evidence for a causal link between continental erosion and biological evolution. Geochimica et Cosmochimica Acta, 304, 327–346.

Liu, C.Y., Pogge von Strandmann P. A.E., Tarbuck, G., Wilson, D., 2022b. Experimental Investigation of Oxide Leaching Methods for Li Isotopes. Geostandards and Geoanalytical Research, 46(3), 493–518.

Liu, X.F., Liu, X.M., Wang, X.K., Zhai, S.K., Liu, X.Y., 2023a. Dolostone as a reliable tracer of seawater lithium isotope composition. Communications Earth & Environment, 4, 58.

Liu, Y., Li, Y.C., Hou, M.C., Shen, J., Algeo, T.J., Fan, J.X., Zhou, X.L., Chen, Q., Sun, Z.Y., Li, C., 2023b. Terrestrial rather than volcanic mercury inputs to the Yangtze Platform (South China) during the Ordovician-Silurian transition. Global and Planetary Change, 220, 104023.

Longman, J., Mills, B. J.W., Manners, H.R., Gernon, T.M., Palmer, M.R., 2021. Late Ordovician climate change and extinctions driven by elevated volcanic nutrient supply. Nature Geoscience, 14, 924–929.

Lu, K., Mitchell, R.N., Yang, C., Zhou, J.L., Wu, L.G., Wang, X.C., Li, X.H., 2022. Widespread magmatic provinces at the onset of the Sturtian snowball Earth. Earth and Planetary Science Letters, 594, 117736.

Lu, X.Z., Gilleaudeau, G.J., Kendall, B., 2024. Uranium isotopes in non-euxinic shale and carbonate reveal dynamic Katian marine redox conditions accompanying a decrease in biodiversity prior to the Late Ordovician Mass Extinction. Geochimica et Cosmochimica Acta, 364, 22–43.

Ma, T.T., Weynell, M., Li, S.L., Liu, Y.S., Chetelat, B., Zhong, J., Xu, S., Liu, C.Q., 2020. Lithium isotope compositions of the Yangtze River headwaters: Weathering in high-relief catchments. Geochimica et Cosmochimica Acta, 280, 46–65.

McKenzie, N.R., Horton, B.K., Loomis, S.E., Stockli, D.F., Planavsky, N.J., Lee, C.T.A., 2016. Continental arc volcanism as the principal driver of icehouse-greenhouse variability. Science, 2016, 352(6284), 444–447.

Melchin, M.J., Mitchell, C.E., Holmden, C., Storch, P., 2013. Environmental changes

in the Late Ordovician–Early Silurian: Review and new insights from black shales and nitrogen isotopes. Geological Society of America Bulletin, 125, 1635–1670.

Michalopoulos, P., Aller, R.C., 1995, Rapid clay mineral formation in Amazon delta sediments: Reverse weathering and oceanic elemental cycles. Science, 270, 614–617.

Misra, S., Froelich, P.N., 2012. Lithium isotope history of Cenozoic seawater: Changes in silicate weathering and reverse weathering. Science, 335, 818–823.

Moreau, J., 2011, The Late Ordovician deglaciation sequence of the SW Murzuq Basin (Libya). Basin Research, 23, 449–477.

Murphy, J.G., Ahm, A.C., Swart, P.K., Higgins, J.A., 2022. Reconstructing the lithium isotopic composition (δ^7Li) of seawater from shallow marine carbonate sediments. Geochimica et Cosmochimica Acta, 337, 140–154.

Myrow, P.M., Fike, D.A., Malmskog, E., Leslie, S.A., Zhang, T.R., Singh, B.P., Chaubey, R.S., Prasad, S.K., 2019. Ordovician–Silurian boundary strata of the Indian Himalaya: Record of the latest Ordovician Boda event. Geological Society of America Bulletin, 131(5/6), 881–898.

Pogge von Strandmann P.A.E., Desrochers A., Murphy M.J., Finlay A.J., Selby D., Lenton T. M., 2017a. Global climate stabilisation by chemical weathering during the Hirnantian glaciation. Geochemical Perspectives Letters, 3, 230–237.

Pogge von Strandmann P.A.E., Schmidt, D.N., Planavsky, N.J., Wei, G.Y., Jones, C.L.C., Baumann, K.H., 2019a. Assessing bulk carbonates as archives for seawater Li isotope ratios. Chemical Geology, 530, 119338.

Pogge von Strandmann P.A.E., Fraser W.T., Hammond, S.J., Tarbuck, G., Wood, I.G., Oelkers, E.H., Murphy, M.J., 2019b. Experimental determination of Li isotope behaviour during basalt weathering. Chemical Geology, 517, 34–43.

Pogge von Strandmann P.A.E., Jenkyns, H.C., Woodfine, R.G., 2013. Lithium isotope evidence for enhanced weathering during Oceanic Anoxic Event 2. Nature Geoscience, 6, 668–672.

Pogge von Strandmann, P.A.E., Vaks, A., Bar-Matthews, M., Ayalon, A., Jacob, E., Henderson, G.M., 2017b. Lithium isotopes in speleothems: temperature-

controlled variation in silicate weathering during glacial cycles. Earth and Planetary Science Letters, 469, 64–74.

Pogge von Strandmann, P.A.E., Jones, M.T., West, A.J., Murphy, M.J., Stokke, E.W., Tarbuck, G., Wilson, D.J., Pearce, C.R., Schmidt, D.N., 2021. Lithium isotope evidence for enhanced weathering and erosion during the Paleocene-Eocene Thermal Maximum. Science Advances, 7, eabh4224.

Pogge von Strandmann, P.A.E., Kasemann, S.A., Wimpenny, J.B., 2020. Lithium and lithium isotopes in Earth's surface cycles. Elements, 16, 253–258.

Pyle, D.M., Mather, T.A., 2003. The importance of volcanic emissions for the global atmospheric mercury cycle. Atmospheric Environment, 37, 5115–5124.

Qiu, Z., Wei, H.Y., Li, T., Corso, J.D., Zhang, J.Q., Zou, C.N., 2022. Different controls on the Hg spikes linked the two pulses of the Late Ordovician mass extinction in South China. Scientific Reports, 12, 5195.

Qiu, Z., Zou, C.N., Mills, B.J.W., Xiong, Y.J., Tao, H.F., Lu, B., Liu, H.L., Xiao, W.J., Poulton, S.W., A nutrient control on expanded anoxia and global cooling during the Late Ordovician mass extinction. Communications Earth & Environment, 3(1), 82.

Rudnick, R.L., Gao, S., 2014. 4.1 – composition of the continental crust. In: Holland, H.D., Turekian, K.K. (Eds.), Treatise on Geochemistry, 2nd ed. Elsevier, Oxford, 1–51.

Sanberg, P.A., Hudson, J.D., 1983. Aragonite relic preservation in Jurassic calcite-replaced bivalves. Sedimentology, 30(6), 879–892.

Sial, A., Chen, J.B., Peralta, S.H., Gaucher, C., Korte, C., Ferreira, V.P., Lacerda, L.D., Barbosa, J.A., Pereira, N.S., Riedel, P.R., Gómez, J., 2024. C, N, Hg isotopes and elemental chemostratigraphy across the Ordovician–Silurian transition in the Argentine Precordillera: Implications for the link between volcanism and extinctions. Gondwana Research, 133, 270–296.

Shen, J., Algeo T.J., Feng Q.L., 2022a. Mercury isotope evidence for a non-volcanic origin of Hg spikes at the Ordovician-Silurian boundary, South China. Earth and Planetary Science Letters, 594, 117705.

Shen, J., Algeo, T.J., Chen, J., Planavsky, N.J., Feng, Q., Yu, J., Liu, J., 2019. Mercury in marine Ordovician/Silurian boundary sections of South China is sulfide-hosted and non-volcanic in origin. Earth and Planetary Science Letters, 511, 130–140.

Shen, J., Yin, R., Algeo, T.J., Svensen, H.H., Schoepfer, S.D., 2022b. Mercury evidence for combustion of organic-rich sediments during the end-Triassic crisis. Nature Communications, 13, 1307.

Smolarek-Lach, J., Marynowski, L., Trela, W., Wignall, P.B., 2019, Mercury spikes indicate a volcanic trigger for the Late Ordovician mass extinction event: An example from a deep shelf of the Peri-Baltic region: Scientific Reports, 9, 3139.

Sproson, A.D., Pogge von Strandmann, P.A.E., Selby, D., Jarochowska, E., Frýda, J., Hladil, J., Loydell, D.K., Slavík, L., Calner, M., Maier, G., Munnecke, A., Lenton, T.M., 2022. Osmium and lithium isotope evidence for weathering feedbacks linked to orbitally paced organic carbon burial and Silurian glaciations. Earth and Planetary Science Letters, 577, 117260.

Su, W.B., Huff, W.D., Ettensohn, F.R., Liu, X.M., Zhang, J.E., Li, Z.M., 2009. K-bentonite, black-shale and flysch successions at the Ordovician-Silurian transition, South China: possible sedimentary responses to the accretion of Cathaysia to the Yangtze Block and its implications for the evolution of Gondwana. Gondwana Research, 15 (1), 111–130.

Swanson-Hysell, N.L., and Macdonald, F.A., 2017. Tropical weathering of the Taconic orogeny asa driver for Ordovician cooling. Geology, 45, 719–722.

Tissot, F.L.H., Dauphas, N., 2015. Uranium isotopic compositions of the crust and ocean: Age corrections, U budget and global extent of modern anoxia. Geochimica et Cosmochimica Acta, 167, 113–143.

Tang, D. J., Fu, X. W., Shi, X. Y., Zhou, L. M., Zheng, W., Li, C., Xu, D.T., Zhou, X.Q., Xie, B.Z., Zhu, X.Y., Jiang, G.Q., 2022. Enhanced weathering triggered the transient oxygenation event at ~1.57 Ga. Geophysical Research Letters, 49(15), e2022GL099018.

van Staal, C., Barr, S., 2012, Lithospheric architecture and tectonic evolution of the Canadian Appalachians and associated Atlantic margin, in Percival, J.A., et al.,

eds., Tectonic styles in Canada: The Lithoprobe perspective: Geological Association of Canada Special Paper, 49, 41–96.

Walker, J.C.G., Hays, P.B., Kasting, J.F., 1981. A negative feedback mechanism for the long-term stabilization of earth's surface temperature. Geophysical Research Letters, 86, 9776–9782.

Wan, S.M., Clift, P.D., Li, A.C., Yu, Z. J., Li, T.G., Hu, D.K., 2012. Tectonic and climatic controls on long-term silicate weathering in Asia since 5 Ma. Geophysical Research Letters, 39(15), L15611.

Wang, Y., Tan, J.Q., Wang, W.H., Zhou, L., Tang, P., Kang, X, Xie, W.Q., Wang, Z.H., Dick, J., 2023. The influence of Late Ordovician volcanism on the marine environment based on high-resolution mercury data from South China. GSA Bulletin, 135(3/4), 787–798.

Wang, Y.J., Zhang, F.F., Fan, W., Zhang, G., Chen, S., Cawood, P.A., Zhang, A., 2010, Tectonic setting of the South China Block in the early Paleozoic: Resolving intracontinental and ocean closure models from detrital zircon U-Pb geochronology. Tectonics, 29, TC6020.

Wei, G.Y., Zhang, F.F., Yin, Y.S., Lin, Y.B., Pogge von Strandmann, P.A.E., Cao, M.C., Li, N., Xiong, G.L., Chen, X.R., Fan, C.W., Xu, C.G., Tan, F., Zhang, X.Y., Yang, H.Q., Ling, H.F., Shen, S.Z., 2023. A 13 million-year record of Li isotope compositions in island carbonates: Constraints on bulk inorganic carbonate as a global seawater Li isotope archive. Geochimica et Cosmochimica Acta, 344, 59-72.

Wei, G.Y., Zhang, F.F., 2024. Pristine or altered, what can early diagenesis tell us in shallow-water carbonates? Earth and Planetary Science Letters, 641, 118806.

Xu, Y., Cawood, P., Du, Y., 2016. Intraplate orogenesis in response to Gondwana assembly: Kwangsian orogeny, South China. American Journal of Science, 316, 329–362.

Yan, D.T., Chen, D.Z., Wang, Q.C., Wang, J.G., 2010, Large-scale climatic fluctuations in the latest Ordovician on the Yangtze block, South China. Geology, 38(7), 599–602.

Yan, D.T., Chen, D.Z., Wang, Q.C., Wang, J.G., Wang, Z.Z., 2009. Carbon and sulfur isotopic anomalies across the Ordovician-Silurian boundary on the Yangtze Platform, South China. Palaeogeography, Palaeoclimatology, Palaeoecology, 274, 32–39.

Yang, J.H., Cawood, P.A., Du, Y.S., Condon, D.J., Yan, J.X., Liu, J.Z., Huang, Y., Yuan, D.X., 2018. Early Wuchiapingian cooling linked to Emeishan basaltic weathering? Earth and Planetary Science Letters, 492, 102–111.

Yang, J.H., Cawood, P.A., Montañez, I.P., Condon, D.J., Du, Y.S., Yan, J.X., Yan, S.Q., Yuan, D.X., 2020. Enhanced continental weathering and large igneous province induced climate warming at the Permo-Carboniferous transition. Earth and Planetary Science Letters, 2020, 534, 116074.

Yang, S.C., Hu, W.X., Fan, J.X., Deng, Y.Y., 2022. New geochemical identification fingerprints of volcanism during the Ordovician-Silurian transition and its implications for biological and environmental evolution. Earth-Science Reviews, 228, 104016.

Yang, S.C., Hu, W.X., Wang, X.L., Jiang, B.Y., Yao, S.P., Sun, F.N., Huang, Z.C., Zhu, F., 2019. Duration, evolution, and implications of volcanic activity across the Ordovician-Silurian transition in the Lower Yangtze region, South China. Earth and Planetary Science Letters, 518, 13–25.

Yang, X.R., Yan, D.T., Chen, D.Z., Liu, M., She, X.H., Zhang, B., Zhang, L.W., Zhang, J.F., 2021. Spatiotemporal variations of sedimentary carbon and nitrogen isotopic compositions in the Yangtze Shelf Sea across the Ordovician-Silurian boundary. Palaeogeography, Palaeoclimatology, Palaeoecology, 567, 110257.

Yang, X.R., Yan, D.T., Zhang, B, Zhang, L., 2023. Anomalous weathering trends during the Early Silurian warming: Implications for the biotic crisis and recovery. Palaeogeography, Palaeoclimatology, Palaeoecology, 111859.

Yang, X.R., Yan, D.T., Liu, M., Liu, X.Y., Gong, Y., Zhang, L.W., Zhang, B., Chen, D.Z., 2024. Zinc isotopic evidence for enhanced continental weathering and organic carbon burial in the Early Silurian. Chemical Geology, 662, 122209.

Young, S.A., Saltzman, M.R., Ausich, W.I., Desrochers, A., Kaljo, D., 2010. Did

changes in atmospheric CO_2 coincide with latest Ordovician glacial-interglacial cycles? Palaeogeography, Palaeoclimatology, Palaeoecology, 296, 376–388.

Young, S.A., Saltzman, M.R., Foland, K.A., Linder, J.S., Kump, L.R., 2009. A major drop in seawater $^{87}Sr/^{86}Sr$ during the Middle Ordovician (Darriwilian): Links to volcanism and climate? Geology, 37(10), 951–954.

Zhou, Y.P., Li, Y., Zheng, W., Tang, S.L., Pan, S. Q., Chen, J.B., He, X.F., Shen, J., Algeo, T.J., 2024. The role of LIPs in Phanerozoic mass extinctions: An Hg perspective. Earth-Science Reviews, 249, 104667.

Zou, C.N., Qiu, Z., Poulton, S. W., Dong, D.Z., Wang, H.Y., Chen, D.Z., Liu, B., Shi, Z.S., Tao, H.F., 2018. Ocean euxinia and climate change "double whammy" drove the Late Ordovician mass extinction. Geology, 46, 535–538.

Zhang, Y., Jaeglé, L., Thompson, L., 2014. Natural biogeochemical cycle of mercury in a global three-dimensional ocean tracer model. Glob. Biogeochem. Cycles 28 (5), 553–570.

Zhang, Y.C., Tang, P., Jin, J.S., Sun, S., Zhang, X.L., Huang, P., Sun, J., Wang, Y., 2021. Climate change in the subtropical Paleo-Tethys before the late Ordovician glaciation. Global and Planetary Change, 199, 103432.

Table captions

Table 1. Carbonate Li isotopes (δ^7Li_{carb}) and trace element ratios, including Al/Ca, Sr/(Ca + Mg), Mg/(Ca + Mg), Mn/Ca, Li/(Mg + Ca), from leaching of the carbonate fraction, and $\delta^{13}C_{org}$ values in the Wukemuchang section.

Table 2. Hg, TOC, TS, and Al_2O_3 concentrations, and Hg/TOC, Hg/TS, and Hg/Al_2O_3 ratios, in bulk rocks from the Wukemuchang section.

Table 1

Sample	Height (m)	Formation	δ^7Li_{carb}	2sd	$\delta^{13}C_{org}$ (‰)	Al/Ca (mmol/mol)	Sr/(Ca+Mg) (mmol/mol)	Mg/(Ca+Mg) (mmol/mol)	Mn/Ca (mmol/mol)	Li/(Ca+Mg) (μmol/mol)
w1	-0.50	Tiezufeike	13.7	0.4	n.d.	0.50	0.33	13.17	0.26	35.51
w2	0.00	Tiezufeike	14.7	0.3	-28.3	0.56	0.54	24.77	0.23	30.36
w3	0.20	Tiezufeike	15.0	0.5	-29.1	0.13	0.46	20.19	0.20	15.25
w4	0.60	Tiezufeike	15.1	0.1	-29.1	0.54	0.54	20.32	0.20	12.55
w5	0.85	Tiezufeike	14.2	0.4	-29.4	0.43	0.39	15.07	0.22	33.81
w6	1.10	Tiezufeike	15.7	0.1	-28.8	0.54	0.57	17.11	0.19	36.18
w7	1.50	Tiezufeike	14.5	0.4	-28.6	0.37	0.47	16.33	0.21	29.77
w8	1.90	Tiezufeike	14.9	0.3	-29.8	0.54	0.51	15.93	0.19	46.22
w9	2.30	Tiezufeike	14.4	0.3	-29.0	0.15	0.49	16.51	0.10	27.48
w10	2.40	Tiezufeike	14.5	0.5	-29.0	0.26	0.28	13.22	0.09	19.92
w11	2.80	Tiezufeike	15.0	0.1	-28.8	0.48	0.27	12.35	0.20	34.13
w12	2.90	Tiezufeike	14.9	0.2	-28.8	0.25	0.66	24.72	0.17	37.37
w13	3.40	Tiezufeike	14.3	0.4	-28.8	0.31	0.61	27.33	0.22	43.52
w14	4.20	Tiezufeike	n.d.	n.d.	-28.9	n.d.	n.d.	n.d.	n.d.	n.d.
w15	4.20	Tiezufeike	15.9	0.1	-27.9	0.65	0.56	35.66	0.24	28.82
w16	4.55	Tiezufeike	15.6	0.1	-28.3	0.48	0.56	17.54	0.25	20.65
w17	4.95	Tiezufeike	14.9	0.3	-28.3	0.26	0.56	21.29	0.11	23.63
w18	5.05	Tiezufeike	13.2	0.2	-28.1	0.67	0.72	20.09	0.25	10.00
w19	5.15	Tiezufeike	11.8	0.3	-28.1	0.62	0.62	16.63	0.28	51.50
w20	5.55	Tiezufeike	12.2	0.1	-28.1	0.57	0.68	18.11	0.25	25.72
w21	6.35	Tiezufeike	13.5	0.2	-28.6	0.54	0.34	17.93	0.22	32.95
w22	6.95	Tiezufeike	12.1	0.3	-28.2	0.19	0.40	12.37	0.12	48.18
w23	7.35	Tiezufeike	14.1	0.1	-28.7	0.64	0.66	34.70	0.16	20.28

w24	7.95	Tiezufeike	15.3	0.2	-27.6	0.31	0.41	27.16	0.25	23.56
w25	8.55	Tiezufeike	16.6	0.2	-27.7	0.52	0.44	15.58	0.29	12.58
w26	9.30	Tiezufeike	15.5	0.1	-27.6	0.36	0.39	49.75	0.30	18.26
w27	9.35	Tiezufeike	9.9	0.1	-27.7	0.47	0.34	11.77	0.19	2.34
w28	9.45	Tiezufeike	10.5	0.2	-27.5	0.47	0.39	14.29	0.18	4.80
w29	9.55	Tiezufeike	10.3	0.3	-26.6	0.49	0.35	9.68	0.18	4.01
w30	9.65	Tiezufeike	12.8	0.2	-26.2	0.45	0.35	12.07	0.23	8.22
w31	9.75	Tiezufeike	14.3	0.2	-25.3	0.58	0.49	12.84	0.20	42.56
w32	9.85	Tiezufeike	14.1	0.2	-26.2	0.56	0.45	13.94	0.21	18.33
w33	10.15	Tiezufeike	15.4	0.3	-26.5	0.18	0.51	16.16	0.09	23.73
w34	10.40	Tiezufeike	15.7	0.1	-28.3	0.25	0.41	15.33	0.11	28.51
w35	10.45	Butuo	9.9	0.2	-28.9	0.17	0.42	16.89	0.04	22.08
w36	10.55	Butuo	9.5	0.2	-28.6	0.10	0.52	16.26	0.03	19.05
w37	10.60	Butuo	10.2	0.4	-29.0	0.48	0.52	10.71	0.27	19.90
w38	10.75	Butuo	12.8	0.2	-29.4	0.07	0.44	13.25	0.05	20.64
w39	11.00	Butuo	10.3	0.2	-29.6	0.21	0.40	15.55	0.04	27.55
w40	11.30	Butuo	10.4	0.2	-29.0	0.15	0.41	14.59	0.03	29.02
w41	11.65	Butuo	10.6	0.4	-29.3	0.13	0.61	17.76	0.04	29.29
w42	12.00	Butuo	11.0	0.1	-30.1	0.12	0.46	13.71	0.04	13.07
w43	12.35	Butuo	12.2	0.5	-30.3	0.28	0.39	15.26	0.05	16.59
w44	12.45	Butuo	10.3	0.2	-30.5	0.18	0.45	17.51	0.03	15.81
w45	12.55	Butuo	9.3	0.4	-30.3	0.53	0.44	23.39	0.13	16.89
w46	12.60	Butuo	12.9	0.6	-30.8	0.37	0.56	21.95	0.31	21.84
w47	12.90	Butuo	9.8	0.5	-30.7	0.14	0.46	18.05	0.05	25.16
w48	13.28	Butuo	11.4	0.3	-30.7	0.08	0.42	20.85	0.13	28.29
w49	13.48	Butuo	15.6	0.3	-30.7	0.48	0.34	9.88	0.26	37.53

w50	14.00	Butuo	14.9	0.3	-30.9	0.26	0.39	10.99	0.19	24.85
w51	14.28	Butuo	14.6	0.6	-30.8	0.19	0.40	12.37	0.12	21.74
w52	14.50	Butuo	15.7	0.4	-30.7	0.39	0.58	18.97	0.28	32.13
w53	14.80	Butuo	n.d.	n.d.	-30.5	n.d.	n.d.	n.d.	n.d.	n.d.
w54	16.10	Butuo	15.1	0.1	-30.2	0.22	0.42	12.27	0.17	17.47
w55	16.50	Butuo	n.d.	n.d.	-30.3	n.d.	n.d.	n.d.	n.d.	n.d.
w56	16.70	Butuo	n.d.	n.d.	-29.4	n.d.	n.d.	n.d.	n.d.	n.d.
w57	17.55	Butuo	15.4	0.3	-29.6	0.32	0.56	28.16	0.32	23.36
w58	18.65	Butuo	15.8	0.5	-29.8	0.45	0.37	12.19	0.26	18.62
w59	19.75	Butuo	n.d.	n.d.	-29.3	n.d.	n.d.	n.d.	n.d.	n.d.
w60	19.95	Butuo	n.d.	n.d.	-29.4	n.d.	n.d.	n.d.	n.d.	n.d.
w61	21.55	Butuo	13.9	0.4	-29.1	0.23	0.67	12.35	0.24	17.04
w62	22.25	Butuo	14.7	0.2	-29.0	0.43	0.80	19.77	0.25	24.14
w63	25.95	Butuo	n.d.	n.d.	-29.8	n.d.	n.d.	n.d.	n.d.	n.d.
w64	26.20	Butuo	n.d.	n.d.	-29.7	n.d.	n.d.	n.d.	n.d.	n.d.

n.d.: not determined

Table 2

Sample	Height (m)	Formation	Hg (ppb)	TOC (%)	TS (%)	Al_2O_3 (%)	Hg/TOC (ppb/%)	Hg/TS (ppb/%)	Hg/Al_2O_3 (ppb/%)
w1	-0.5	Tiezufeike	12	0.11	0.02	n.d.	107	588.6	n.d.
w2	0	Tiezufeike	14	0.13	0.03	0.97	110.4	473.4	14.64
w3	0.2	Tiezufeike	9	0.1	0.01	0.26	94.1	905	34.81
w4	0.6	Tiezufeike	17	0.21	0.02	1.47	82.1	852.1	11.59
w5	0.85	Tiezufeike	19	0.16	0.03	0.51	123.8	642	37.76
w6	1.1	Tiezufeike	13	0.17	0.01	1.05	77.2	1292.3	12.33
w7	1.5	Tiezufeike	19	0.22	0.01	1.89	86.5	1900.9	10.04
w8	1.9	Tiezufeike	12	0.19	0.02	1.45	61.7	597.8	8.22
w9	2.3	Tiezufeike	33	0.38	0.03	15.17	86.7	1095	2.17
w10	2.4	Tiezufeike	12	0.14	0.01	1.51	84.5	1206	7.99
w11	2.8	Tiezufeike	9	0.11	0.01	0.08	82.7	913.3	109.29
w12	2.9	Tiezufeike	8	0.16	0.01	4.82	51.7	844	1.75
w13	3.4	Tiezufeike	43	0.33	0.03	4.63	128.7	1430.2	9.27
w15	4.2	Tiezufeike	15	0.28	0.02	2.22	53.4	738.3	6.64
w16	4.55	Tiezufeike	14	0.2	0.02	2.19	71.5	716.1	6.55
w17	4.95	Tiezufeike	16	0.31	0.02	1.87	50.8	794.5	8.48
w18	5.05	Tiezufeike	21	0.29	0.02	3.01	73	1057.6	7.03
w19	5.15	Tiezufeike	36	0.18	0.01	4.83	201.4	3556.5	7.36
w20	5.55	Tiezufeike	14	0.09	0.01	0.25	158.6	1413	56.05
w21	6.35	Tiezufeike	24	0.34	0.03	1.89	71.7	808.9	12.86
w22	6.95	Tiezufeike	202	1.04	0.04	1.52	193.9	5041	132.36
w23	7.35	Tiezufeike	273	1.39	0.01	1.15	196.4	27324.2	238.57

w24	7.95	Tiezufeike	16	0.14	0.01	0.65	112.5	1571	24.09
w25	8.55	Tiezufeike	15	0.15	0.02	1.15	98.8	742.3	12.86
w26	9.3	Tiezufeike	n.d.	0.15	0.03	1.51	n.d.	n.d.	6.81
w27	9.35	Tiezufeike	3	0.05	0.01	n.d.	57.9	289.3	n.d.
w28	9.45	Tiezufeike	5	0.07	0.01	0.5	68.3	478.4	9.57
w29	9.55	Tiezufeike	8	0.1	0.02	0.48	80.6	403	16.91
w30	9.65	Tiezufeike	7	0.15	0.01	n.d.	45.2	688.6	n.d.
w31	9.75	Tiezufeike	8	0.11	0.02	1.28	68.6	377.5	5.91
w32	9.85	Tiezufeike	8	0.16	0.02	n.d.	53.1	424.6	n.d.
w33	10.15	Tiezufeike	16	0.27	0.03	2.63	59.8	537.9	6.14
w34	10.4	Tiezufeike	12	0.11	0.02	1.76	105.9	599.2	6.81
w35	10.45	Butuo	5	0.15	0.03	0.85	33.9	169.5	5.95
w36	10.55	Butuo	6	0.11	0.04	0.42	52.7	144.8	13.72
w37	10.6	Butuo	5	0.12	0.03	7.3	41.6	166.4	0.68
w38	10.75	Butuo	33	0.51	0.02	0.63	64.3	1639.4	51.84
w39	11	Butuo	20	0.37	0.03	0.39	54.3	669.6	51.98
w40	11.3	Butuo	n.d.	n.d.	n.d.	n.d.	n.d.	n.d.	n.d.
w41	11.65	Butuo	12	0.16	0.01	0.52	75.1	1201.1	22.97
w42	12	Butuo	14	0.23	0.01	0.36	60.5	1391.3	38.67
w43	12.35	Butuo	21	0.25	0.02	n.d.	n.d.	n.d.	n.d.
w44	12.45	Butuo	18	0.44	0.04	0.34	40.6	446.7	53.26
w45	12.55	Butuo	19	0.63	0.06	0.27	30.3	319.6	70.34
w46	12.6	Butuo	n.d.	1.48	0.15	n.d.	n.d.	n.d.	n.d.
w47	12.9	Butuo	5	0.15	0.06	n.d.	34.2	85.4	n.d.
w48	13.28	Butuo	19	0.3	0.03	0.31	63.2	631.6	60.79
w49	13.48	Butuo	75	0.8	0.01	2.51	93.7	7495.3	29.86

w50	14	Butuo	43	0.62	0.02	1.85	68.8	2145	23.25
w51	14.28	Butuo	25	0.51	0.07	1.14	48.6	354	21.67
w52	14.5	Butuo	90	2.29	0.44	n.d.	39.3	204.8	n.d.
w53	14.8	Butuo	47	0.47	0.07	2.12	99.2	666.2	21.96
w54	16.1	Butuo	n.d.	0.49	0.1	n.d.	n.d.	n.d.	n.d.
w55	16.5	Butuo	7	0.14	0.05	0.52	49.1	137.6	13.33
w56	16.7	Butuo	102	2.25	0.46	6.28	45.3	221.6	16.23
w57	17.55	Butuo	38	2.1	0.35	7.78	18	108.1	4.86
w58	18.65	Butuo	113	2.3	0.44	8.04	49.1	256.9	14.06
w59	19.75	Butuo	3	0.11	0.09	n.d.	28.4	34.7	n.d.
w60	19.95	Butuo	24	0.63	0.08	0.63	37.7	296.5	37.51
w61	21.55	Butuo	22	0.86	0.03	n.d.	25.7	736.4	n.d.
w62	22.25	Butuo	37	1.18	0.56	5.29	31.7	66.8	7.06
w63	25.95	Butuo	28	0.89	0.11	3.83	31.4	254	7.29
w64	26.2	Butuo	20	0.73	0.24	3.33	27.7	84.3	6.08

n.d.: not determined

Figure captions

Figure 1. (A) Palaeogeographic map of the late Ordovician period (~440 Ma, http://deeptimemaps.com), showing the locations of the South China sections (red dot) and other global sections: (1) Pointe Laframboise, Anticosti Island, Canada; (2) Ellis Bay West, Anticosti Island, Canada; (3) Dob's Linn, Scotland, UK; (4) Monitor Range, Nevada, USA; (5) Vinini Creek, Nevada, USA; and (6) Holy Cross Mountains, Poland (orange dots). (B) Regional palaeogeographic map, showing the distribution of the lithofacies of the Yangtze Block in the Early Silurian (modified from Chen et al., 2004; Zou et al., 2018) and key sections: Wuke (WK, red star), Wangjiawan (WJW), Muchanggou (MCG), and Borehole XY-5 (red circles). (C) Schematic records of $\delta^{18}O$, $\delta^{13}O$, sea level, graptolite zones, and environmental events (seawater anoxia, warming and cooling events; Melchin et al., 2013) through the OST. Time scale and graptolite zones are from Melchin et al. (2013). LOME 0 represents the Katian extinction, and LOME 1 and LOME 2 represent the first and second phases of the Late Ordovician Mass Extinction (Deng et al., 2021). HICE represents the Hirnantian isotopic carbon excursion. Orange and blue bars represent global warming and cooling events, respectively.

Figure 2. Carbon isotope stratigraphy of the global sections discussed here. Sources for carbon isotope data are as follows: Wangjiawan (Yan et al., 2009), Wuke ($\delta^{13}C_{org:}$ this study; $\delta^{13}C_{carb:}$ Liu et al., 2022a), Dob's Linn (Hammarlund et al., 2012), Pointe Laframboise (Young et al., 2010), Vinini Creek (Hu et al., 2021), Parahio Valley India Himalaya (Myrow et al., 2019). Placement of the Katian–Hirnantian boundary in the Point Laframboise section is based on detailed chitinozoan biostratigraphy and geochemical records (Achab et al., 2011; Kozik et al., 2022b). P represents positive excursion, and N represents negative excursion. Orange and blue bars represent global warming (low $\delta^{13}C$ values) and cooling (high $\delta^{13}C$) events, respectively. GYQ, Guanyinqiao Member; LX, Linxiang Formation.

Figure 3. Cross plots comparing (A) δ^7Li_{carb} values to Al/Ca ratios, (B) δ^7Li_{carb} values to Mn/Ca ratios, (C) Sr/(Ca+Mg) values to Li/(Ca+Mg) ratios, (D) δ^7Li_{carb} values to Li/(Ca+Mg) ratios, (E) δ^7Li_{carb} values to Sr/(Ca+Mg) ratios, and (F) δ^7Li_{carb} values to Mg/(Ca+Mg) ratios. All data are from carbonate leaching. Black arrows indicate the directions along the x-axis in which leaching or diagenetic processes would be expected to shift the elemental ratios. Grey arrows indicate the trend towards four samples (circled and labelled with sample names) with low Sr/(Ca+Mg) ratios, Li/(Ca+Mg) ratios, and δ^7Li values that appear to have experienced meteoric diagenesis (Dellinger et al., 2020; Murphy et al., 2022; Wei et al., 2023).

Figure 4. Comparison of $\delta^{13}C_{carb}$ and $\delta^{18}O$ (Liu et al., 2022a), $\delta^{13}C_{org}$, δ^7Li_{carb} (2SD are better than 0.6‰), Hg/TOC, Hg/TS, Hg/Al_2O_3, $\delta^{238}U_{carb}$ (2SE are better than 0.05‰; Liu et al., 2022a), and mineralogy (Yang et al., 2021) records from Upper Ordovician to Lower Silurian strata in the Wuke section. For U isotopes, we also show the values of $\delta^{238}U_{seawater}$ (~ -0.39‰; Tissot and Dauphas, 2015) and $\delta^{238}U_{Bahamas\ limestones}$ (~ -0.14‰; Chen et al., 2018). The graptolite zones in the Wuke section are according to Liu et al. (2022a). Four samples with Li isotopes that appear to have been affected by meteoric diagenesis (see Fig. 3) are plotted in open grey symbols and not connected by the line. The median values (baseline) of Hg/TOC, Hg/TS, and Hg/Al_2O_3 in the non-volcanic sedimentary rocks are 63 ppb/%, 631 ppb/%, and 13 ppb/%, respectively, while spikes are characterised as higher than 2×baseline. Orange and blue bars represent global warming (low $\delta^{13}C$ values) and cooling (high $\delta^{13}C$) events, respectively. The numbers in red circles labelled 'stage' represent time intervals: 1, late Katian; 2, latest Katian; 3, early Hirnantian; 4, latest Hirnantian; 5, Rhuddanian.

Figure 5. Lithium and carbon isotope records from carbonate and shale sections (this study; Pogge von Strandmann et al., 2017a). The Wuke, Pointe Laframboise, and Ellis Bay West sections are marine carbonates ($\delta^7Li_{carb,}$ analysed on carbonate leachates), while the Dob's Linn section comprises shales ($\delta^7Li_{shale,}$ analysed on bulk shales). For Wuke, four samples with Li isotopes that appear to have been affected by meteoric

diagenesis (see Fig. 3) are plotted in open grey symbols and not connected by the line. Labels Px and Nx represent positive and negative Li isotope excursions, respectively. Time scale and graptolite zones are from Melchin et al. (2013). The numbers in red circles labelled 'stage' represent time intervals: 1, late Katian; 2, latest Katian; 3, early Hirnantian; 4, latest Hirnantian; 5, Rhuddanian.

Figure 6. Summary of environmental parameters and biological evolution across the OST. (A) Seawater Li isotope reconstructions from Pogge von Strandmann et al. (2017a) and this study, with the offset between seawater and carbonate set at ~ 6.1‰ ($\Delta^7Li_{seawater-calcite}$ = 6.1 ± 1.3‰; Pogge von Strandmann et al., 2019a). Red line indicates simplified seawater evolution: late Katian (stage 1, Wuke section, $\delta^7Li_{seawater}$ ~ 21‰), latest Katian (stage 2, Ellis Bay West and Pointe Laframboise sections, $\delta^7Li_{seawater}$ ~ 16‰), early Hirnantian (stage 3, Ellis Bay West and Pointe Laframboise sections, $\delta^7Li_{seawater}$ ~ 24‰), latest Hirnantian (stage 4, Wuke, Ellis Bay West, and Pointe Laframboise sections, $\delta^7Li_{seawater}$ ~ 16‰) and Rhuddanian (stage 5, Wuke section, $\delta^7Li_{seawater}$ ~ 21‰). Intervals of incongruent and congruent weathering are indicated above the curve with arrows. (B) Marine $^{187}Os/^{188}Os$ curve as continental weathering indicator from Finlay et al. (2010). (C) Tropical sea-surface temperature (SST) curve from Finnegan et al. (2011) and Melchin et al. (2013). Orange and blue bars represent the global warming and cooling events, respectively. (D) Uranium (U) and thallium (Tl) isotope records from Liu et al. (2022a) and Kozik et al (2022a); note the reversed y-axis for the Tl record. Pink and brown bars represent expansions of euxinic and anoxic seawater, respectively. (E) Global and local biodiversity curves from Deng et al. (2021) and Fan et al. (2020); note the reversed y-axes. Red bars represent the Late Ordovician Mass Extinctions (LOME 0, LOME 1, LOME 2). (F) Sedimentary Hg anomalies in Wuke (this study), Muchanggou (Wang et al., 2023), Wangjiawan (Jones et al., 2017; Gong et al., 2017), Borehole XY-5 (Hu et al., 2021), Holy Cross Mountains (Smolarek-Lach et al., 2019), Monitor Range (Jones et al., 2017), Vinini Creek (Hu et al., 2021), and Dob's Linn (Bond and Grasby, 2020). Labels indicate a possible switch from volcanism-induced to weathering-induced Hg anomalies. The numbers in red circles at

the top of the figure labelled 'stage' represent time intervals: 1, late Katian; 2, latest Katian; 3, early Hirnantian; 4, latest Hirnantian; 5, Rhuddanian.

Figure 7. (A) Modelled seawater δ^7Li values if $\Delta_{seawater\text{-}sed}$ decreases from 5 to 3.5 (temperature increase of ~10 °C), or from 5 to 0.5‰ (temperature increase of ~30 °C) for 400 kyr. (B) Modelled seawater δ^7Li values for an 8×, 4×, or 2× increase in the hydrothermal flux for 400 kyr. (C) Modelled seawater δ^7Li values if δ^7Li_{riv} decreases from 20‰ to 16‰, 12‰, or 10‰ for 400 kyr. (D) Modelled seawater δ^7Li values for a 4×, 2×, or 0.5× change in the river flux for 400 kyr (with δ^7Li_{riv} fixed at 20‰).

Figure 8. (A) A simplified model for the oceanic Li cycle. (B) The modern-day relationship between weathering intensity (W/D) and δ^7Li_{riv} values (Dellinger et al., 2015), with the proposed positions of time intervals 1-5 shown in red circles. (C) Modelling the OST Li isotope excursions through time. The graph shows the model output (i.e., predicted $\delta^7Li_{seawater}$ values) forced by the imposed changes in temperature and chemical weathering (riverine Li flux and δ^7Li_{riv} values), and by chemical weathering alone (constant temperature). In the model, the initial parameters are based on Pogge von Strandmann et al. (2017a) and Sproson et al. (2022): $F_{riv} = 1.93\times10^{10}$ mol Li/yr; $F_{hyd} = 9\times10^9$ mol Li/yr; $\delta^7Li_{hyd} = 7$‰; $\Delta_{seawater\text{-}sed} = 5$‰ ($\delta^7Li_{seawater} - \delta^7Li_{sed}$); $F_{sed} = 1.5\times10^{10}$ mol Li/yr. The time scale is based on graptolite zones (Melchin et al., 2013; Liu et al., 2022a). Orange bars represent warm climates, and blue bar represents the Hirnantian glaciation. LOME, Late Ordovician Mass Extinctions. The numbers in red circles represent time intervals: 1, late Katian; 2, latest Katian; 3, early Hirnantian; 4, latest Hirnantian; 5, Rhuddanian.

Figure 9. Cross plots comparing Hg concentrations to (A) TOC values, (B) TS values, and (C) Al_2O_3 values. Data are separated into two groups for the Tiezufeike Formation and the Butuo Formation. Two data points in the oval have extremely high Hg contents, and are excluded from the best fit lines.

1480

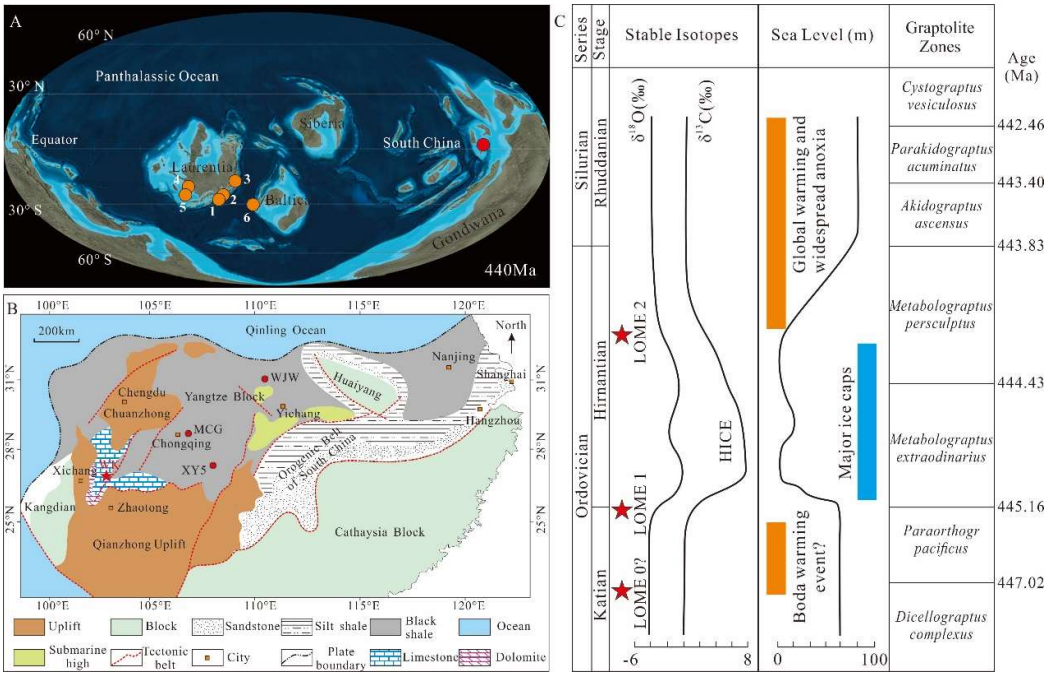
A
60° N
30° N
Equator
30° S
60° S
Panthalassic Ocean
Siberia
South China
Laurentia
Baltica
Gondwana
440Ma
B
200km
Qinling Ocean
North
Nanjing
Shanghai
Chengdu
Chuanzhong
Yangtze Block
WJW
Huaiyang
Yichang
Hangzhou
MCG
Chongqing
Xichang
XY5
Orogenic Belt of South China
Kangdian
Zhaotong
Qianzhong Uplift
Cathaysia Block
Uplift
Block
Sandstone
Silt shale
Black shale
Ocean
Submarine high
Tectonic belt
City
Plate boundary
Limestone
Dolomite
C
Series
Stage
Stable Isotopes
Sea Level (m)
Graptolite Zones
Age (Ma)
Silurian
Rhuddanian
Ordovician
Hirnantian
Katian
δ18O(‰)
δ13C(‰)
LOME 2
LOME 1
LOME 0?
HICE
Global warming and widespread anoxia
Major ice caps
Boda warming event?
-6
8
0
100
Cystograptus vesiculosus
Parakidograptus acuminatus
Akidograptus ascensus
Metabolograptus persculptus
Metabolograptus extraodinarius
Paraorthogr pacificus
Dicellograptus complexus
442.46
443.40
443.83
444.43
445.16
447.02

Figure 1

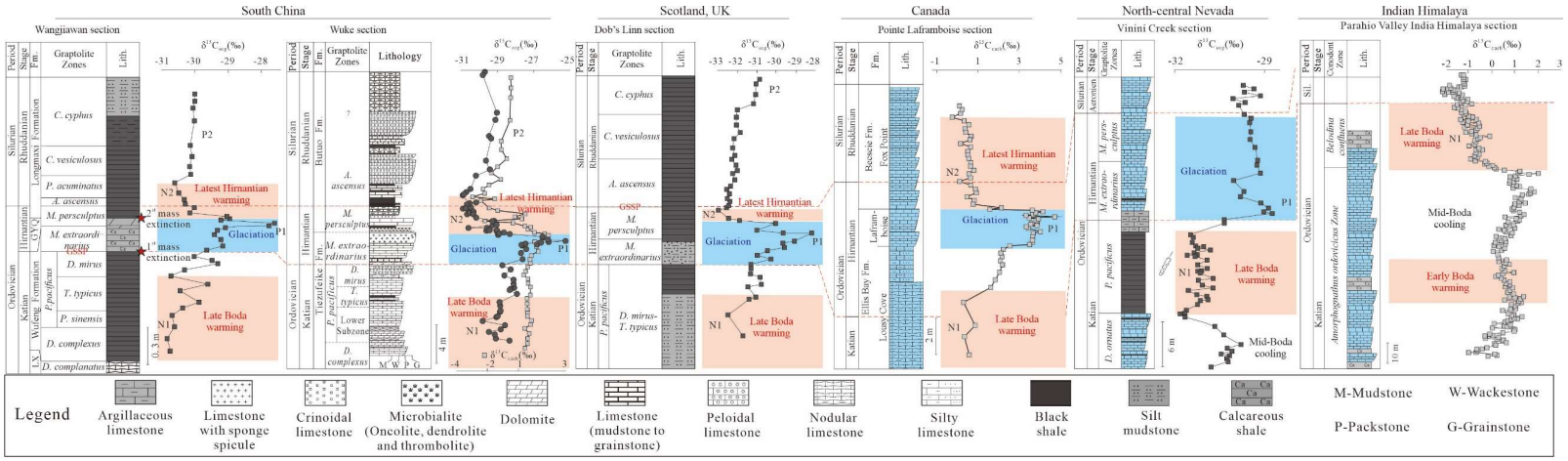
South China
Wangjiawan section
Wuke section
Scotland, UK
Dob's Linn section
Canada
Pointe Laframboise section
North-central Nevada
Vinini Creek section
Indian Himalaya
Parahio Valley India Himalaya section
Latest Hirnantian warming
Glaciation
Late Boda warming
Mid-Boda cooling
Early Boda warming
2nd mass extinction
1st mass extinction
Legend
Argillaceous limestone
Limestone with sponge spicule
Crinoidal limestone
Microbialite (Oncolite, dendrolite and thrombolite)
Dolomite
Limestone (mudstone to grainstone)
Peloidal limestone
Nodular limestone
Silty limestone
Black shale
Silt mudstone
Calcareous shale
M-Mudstone
W-Wackestone
P-Packstone
G-Grainstone

Figure 2

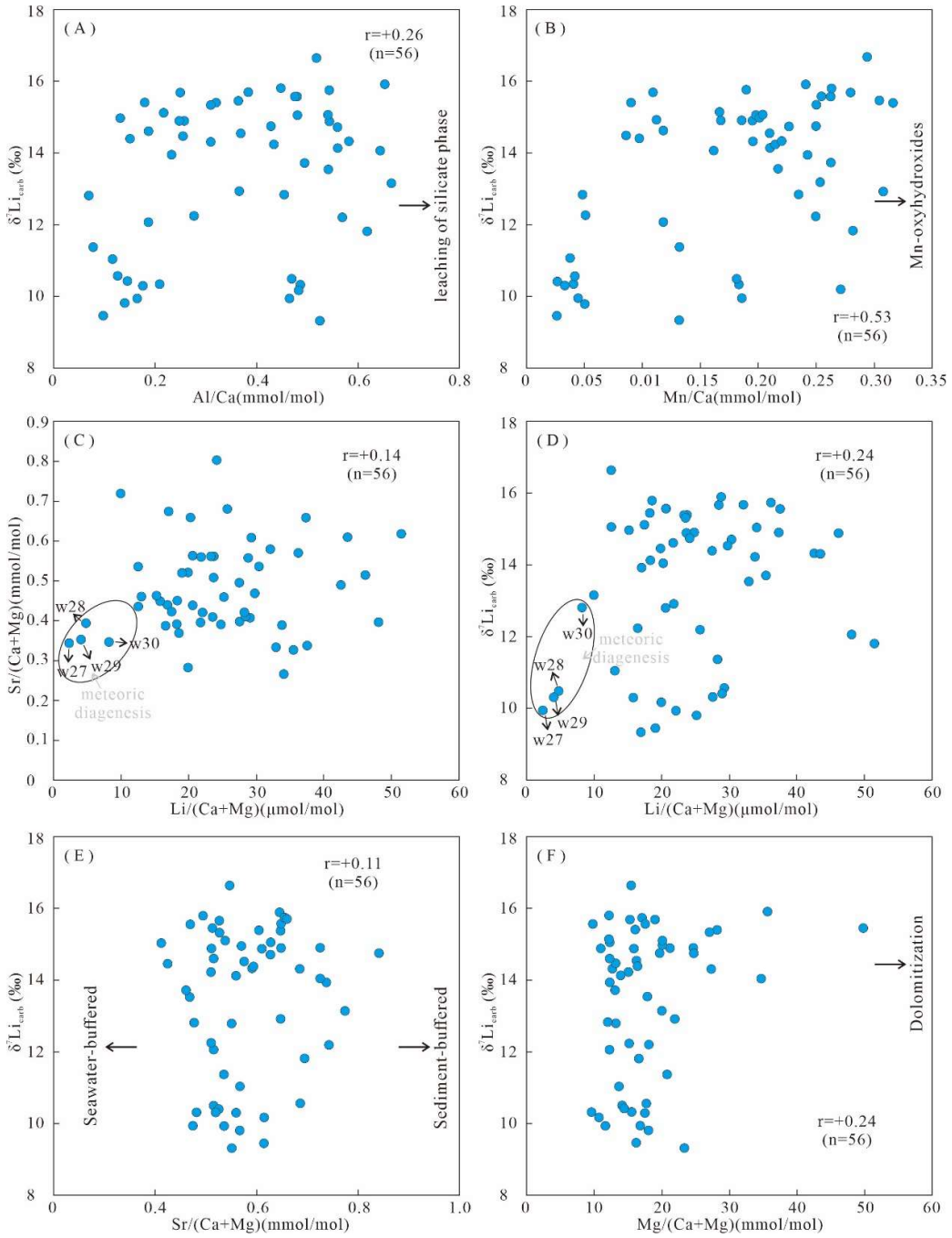
(A)
r=+0.26
(n=56)
leaching of silicate phase
δ7Licarb (‰)
Al/Ca(mmol/mol)
(B)
Mn-oxyhydroxides
r=+0.53
(n=56)
Mn/Ca(mmol/mol)
(C)
r=+0.14
(n=56)
w28
w30
w27
w29
meteoric
diagenesis
Sr/(Ca+Mg)(mmol/mol)
Li/(Ca+Mg)(μmol/mol)
(D)
r=+0.24
(n=56)
w30
w28
w29
w27
meteoric
diagenesis
Li/(Ca+Mg)(μmol/mol)
(E)
r=+0.11
(n=56)
Seawater-buffered
Sediment-buffered
Sr/(Ca+Mg)(mmol/mol)
(F)
Dolomitization
r=+0.24
(n=56)
Mg/(Ca+Mg)(mmol/mol)

Figure 3

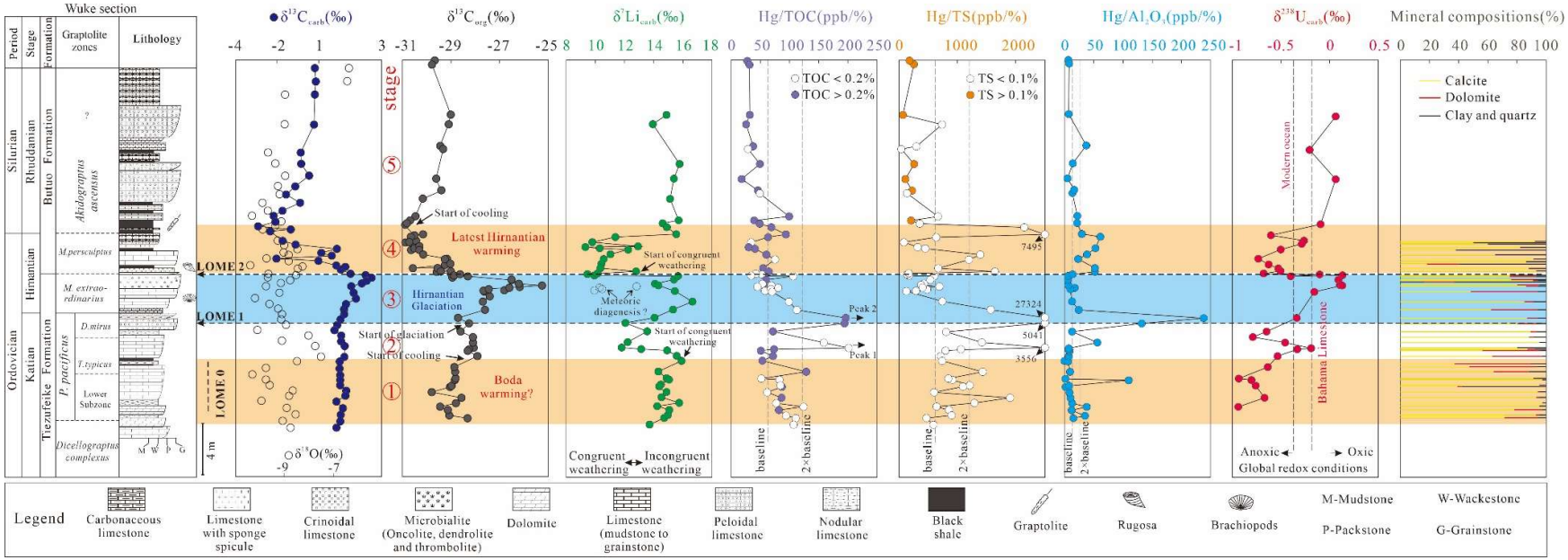
Wuke section
Period
Stage
Formation
Graptolite zones
Lithology
Silurian
Rhuddanian
Butuo Formation
Ordovician
Hirnantian
Katian
Tiezufeike Formation
Akidograptus ascensus
M.persculptus
M. extraordinarius
D.mirus
T.typicus
P. pacificus
Lower Subzone
Dicellograptus complexus
LOME 2
LOME 1
LOME 0
4 m
δ13Ccarb(‰)
δ13Corg(‰)
δ7Licarb(‰)
Hg/TOC(ppb/%)
Hg/TS(ppb/%)
Hg/Al2O3(ppb/%)
δ238Ucarb(‰)
Mineral compositions(%)
δ18O(‰)
stage
Start of cooling
Latest Hirnantian warming
Hirnantian Glaciation
Start of glaciation
Boda warming?
Start of congruent weathering
Meteoric diagenesis?
Congruent weathering
Incongruent weathering
TOC < 0.2%
TOC > 0.2%
Peak 2
Peak 1
baseline
2×baseline
TS < 0.1%
TS > 0.1%
7495
27324
5041
3550
Modern ocean
Bahama Limestone
Anoxic
Oxic
Global redox conditions
Calcite
Dolomite
Clay and quartz
Legend
Carbonaceous limestone
Limestone with sponge spicule
Crinoidal limestone
Microbialite (Oncolite, dendrolite and thrombolite)
Dolomite
Limestone (mudstone to grainstone)
Peloidal limestone
Nodular limestone
Black shale
Graptolite
Rugosa
Brachiopods
M-Mudstone
W-Wackestone
P-Packstone
G-Grainstone

Figure 4

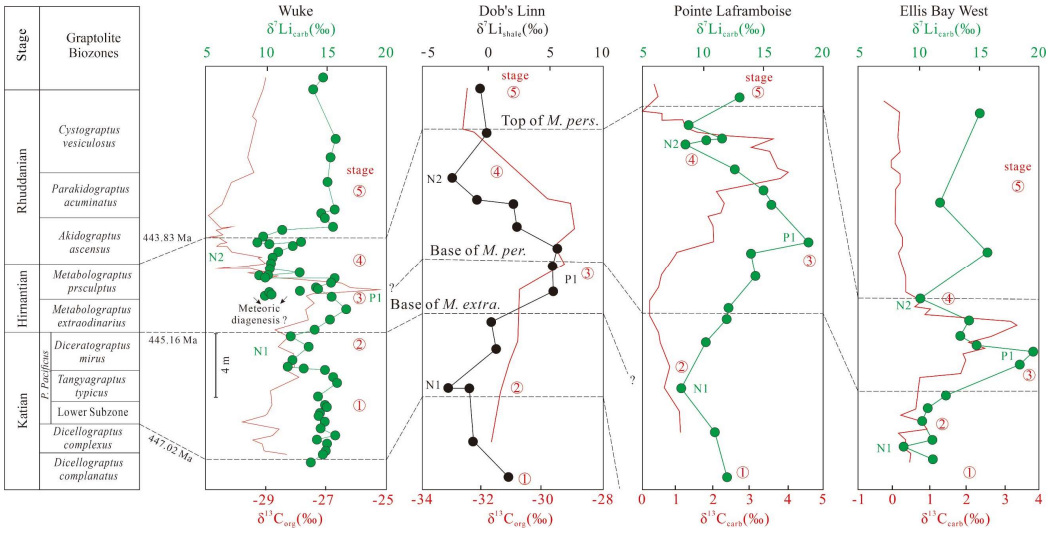
Stage
Graptolite Biozones
Rhuddanian
Hirnantian
Katian
P. Pacificus
Cystograptus vesiculosus
Parakidograptus acuminatus
Akidograptus ascensus
Metabolograptus prsculptus
Metabolograptus extraodinarius
Diceratograptus mirus
Tangyagraptus typicus
Lower Subzone
Dicellograptus complexus
Dicellograptus complanatus
443.83 Ma
445.16 Ma
447.02 Ma
Wuke
Dob's Linn
Pointe Laframboise
Ellis Bay West
δ7Licarb(‰)
δ7Lishale(‰)
δ13Corg(‰)
δ13Ccarb(‰)
stage
Top of M. pers.
Base of M. per.
Base of M. extra.
Meteoric diagenesis ?
4 m
N1
N2
P1

Figure 5

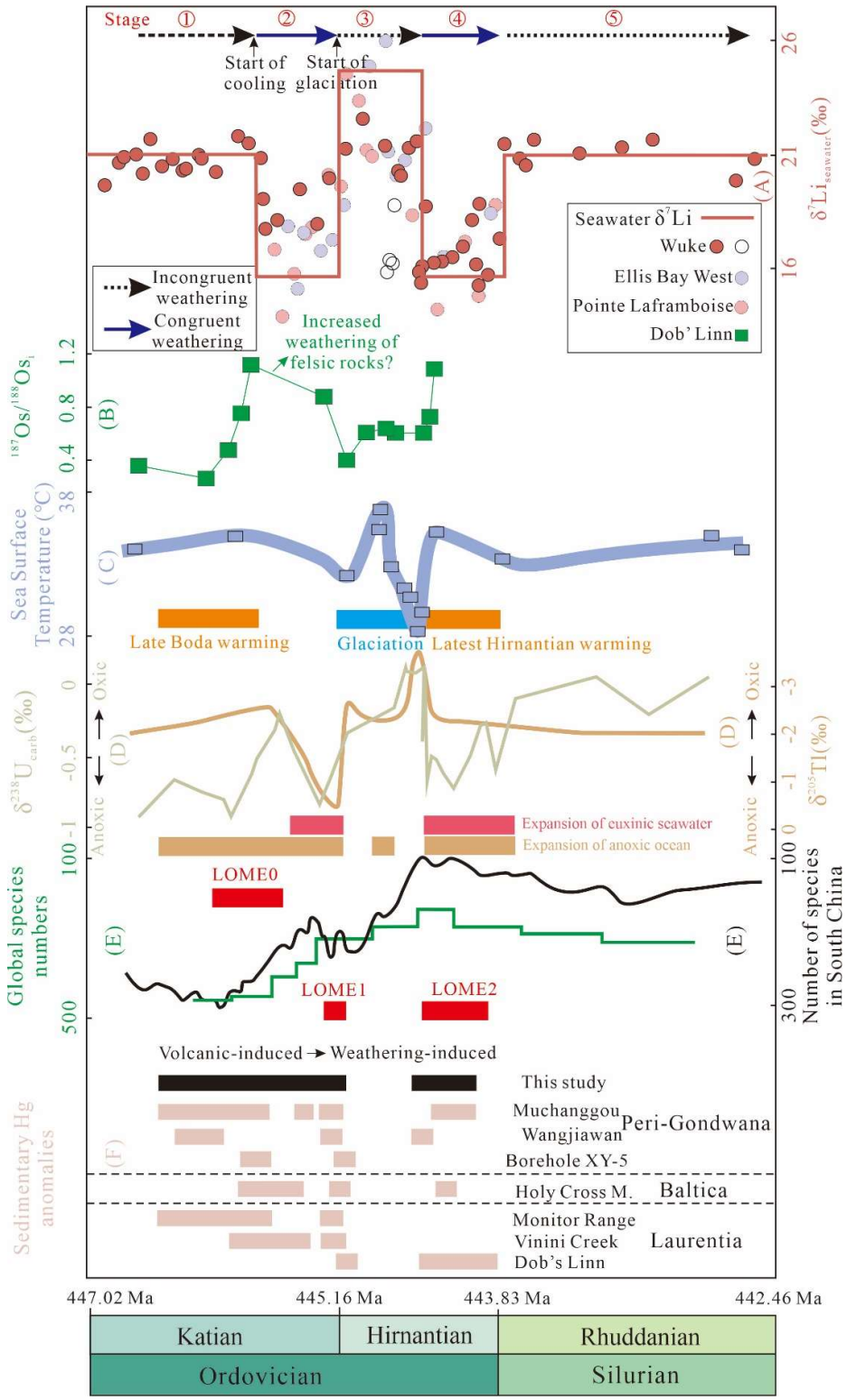
Stage ① ② ③ ④ ⑤
Start of cooling
Start of glaciation
Seawater δ7Li
Wuke
Ellis Bay West
Pointe Laframboise
Dob' Linn
Incongruent weathering
Congruent weathering
Increased weathering of felsic rocks?
(A)
δ7Lis eawater(‰)
26
21
16
(B)
187Os/188Osi
1.2
0.8
0.4
(C)
Sea Surface Temperature (°C)
38
28
Late Boda warming
Glaciation
Latest Hirnantian warming
(D)
δ238Ucarb(‰)
0
-0.5
Oxic
Anoxic
δ205Tl(‰)
-3
-2
-1
0
Expansion of euxinic seawater
Expansion of anoxic ocean
LOME0
LOME1
LOME2
(E)
Global species numbers
100
500
Number of species in South China
300
Volcanic-induced → Weathering-induced
(F)
Sedimentary Hg anomalies
This study
Muchanggou
Wangjiawan
Peri-Gondwana
Borehole XY-5
Holy Cross M.
Baltica
Monitor Range
Vinini Creek
Dob's Linn
Laurentia
447.02 Ma
445.16 Ma
443.83 Ma
442.46 Ma
Katian
Hirnantian
Rhuddanian
Ordovician
Silurian

Figure 6

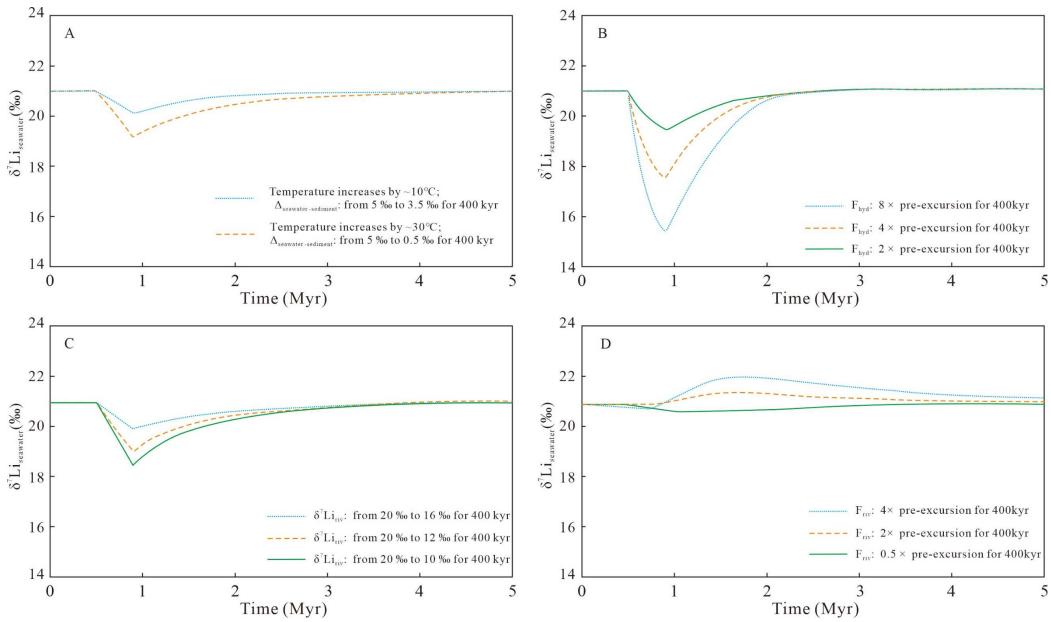
A
B
C
D
Time (Myr)
Temperature increases by ~10°C;
Δseawater-sediment: from 5 ‰ to 3.5 ‰ for 400 kyr
Temperature increases by ~30°C;
Δseawater-sediment: from 5 ‰ to 0.5 ‰ for 400 kyr
Fhyd: 8 × pre-excursion for 400kyr
Fhyd: 4 × pre-excursion for 400kyr
Fhyd: 2 × pre-excursion for 400kyr
δ7Liriv: from 20 ‰ to 16 ‰ for 400 kyr
δ7Liriv: from 20 ‰ to 12 ‰ for 400 kyr
δ7Liriv: from 20 ‰ to 10 ‰ for 400 kyr
Friv: 4× pre-excursion for 400kyr
Friv: 2× pre-excursion for 400kyr
Friv: 0.5 × pre-excursion for 400kyr

Figure 7

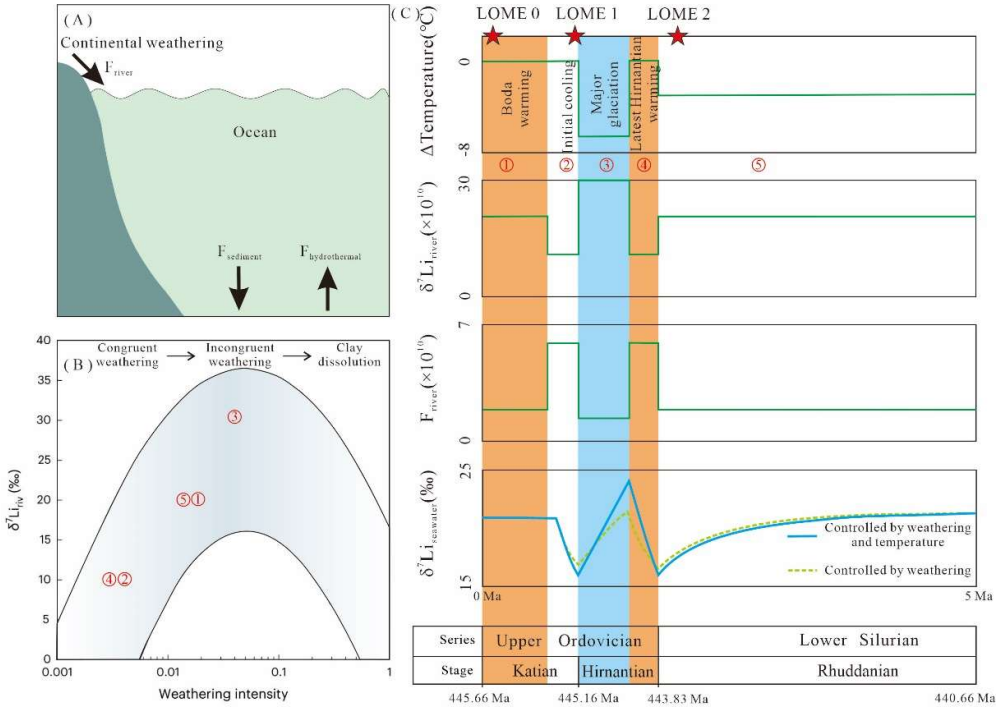
(A)
Continental weathering
F river
Ocean
F sediment
F hydrothermal
(B)
Congruent weathering
Incongruent weathering
Clay dissolution
δ7Liriv (‰)
Weathering intensity
(C)
LOME 0
LOME 1
LOME 2
ΔTemperature(°C)
Boda warming
Initial cooling
Major glaciation
Latest Hirnantian warming
δ7Liriver(×10¹⁰)
Friver(×10¹⁰)
δ7Liseawater(‰)
Controlled by weathering and temperature
Controlled by weathering
0 Ma
5 Ma
Series
Upper Ordovician
Lower Silurian
Stage
Katian
Hirnantian
Rhuddanian
445.66 Ma
445.16 Ma
443.83 Ma
440.66 Ma

Figure 8

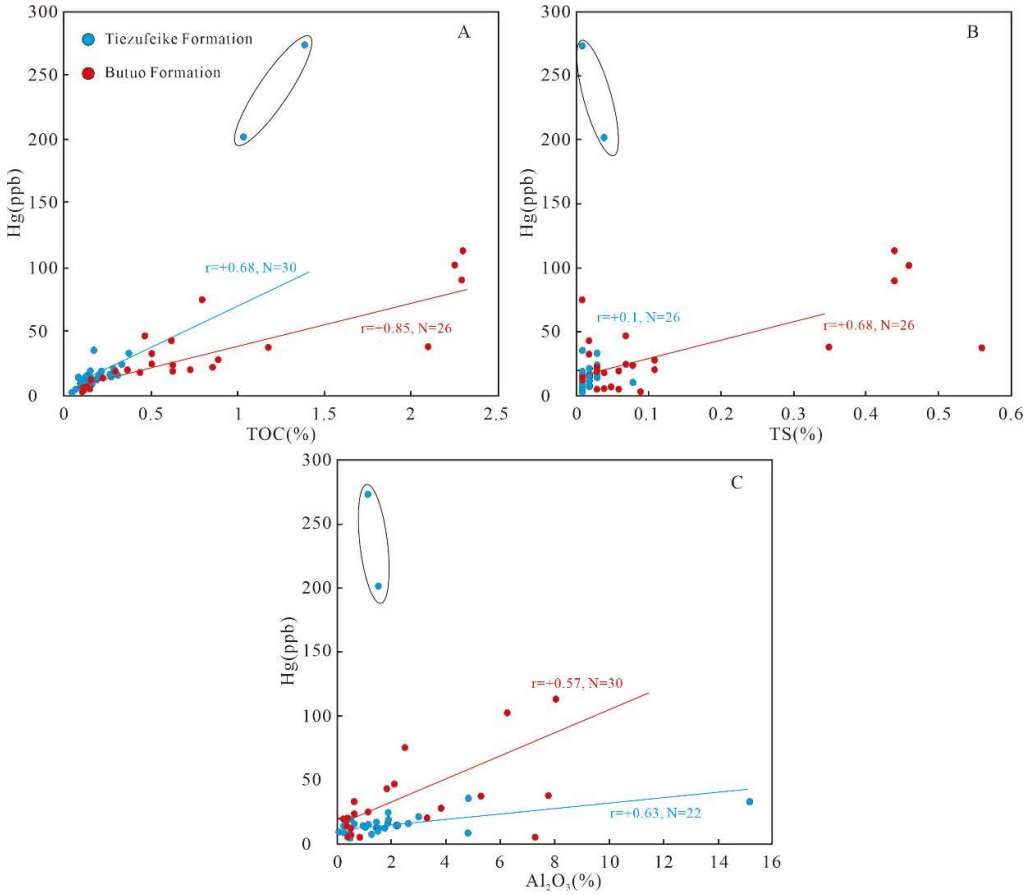
Tiezufeike Formation
Butuo Formation
A
B
C
Hg(ppb)
TOC(%)
TS(%)
Al_2O_3(%)
r=+0.68, N=30
r=+0.85, N=26
r=+0.1, N=26
r=+0.68, N=26
r=+0.57, N=30
r=+0.63, N=22

Figure 9